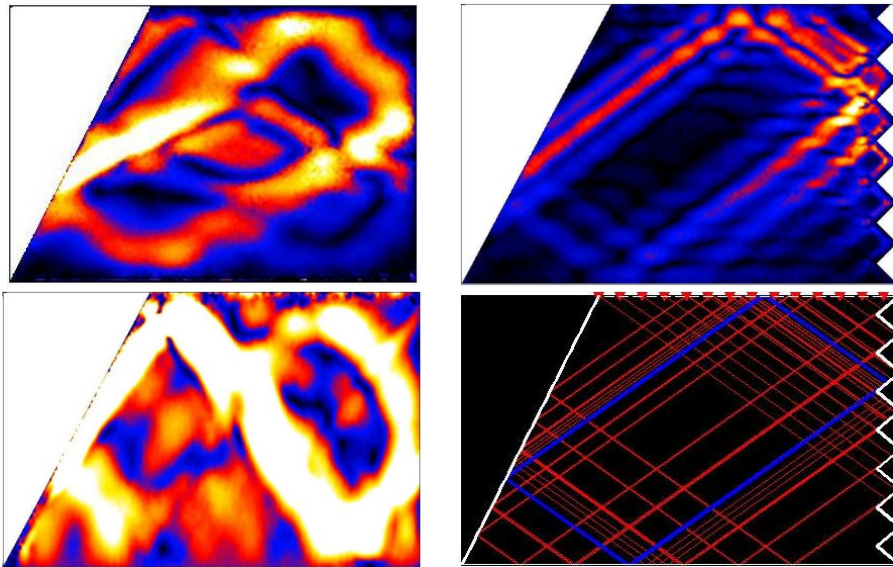**UNIVERSITEIT UTRECHT**

Perturbed Internal Wave Attractors

Laboratory Experiments

Master Thesis Physical Oceanography, Meteorology and Climate
Institute for Marine and Atmospheric research (IMAU)
Faculty of Science, department of Physics and Astronomy

Chrysanthi Tsimitri

Supervised by:
Prof. dr. L.R.M. Maas
drs. J. Hazewinkel

August 2009

Table of Contents

Bibliography

Acknowledgements

Abstract

In this thesis we present a series of laboratory experiments on perturbed internal wave attractors. The internal waves are generated by applying a horizontal harmonic forcing on a two dimensional trapezoidal basin with a sloping wall. To visualize the waves we use the synthetic schlieren technique. We examine the existence and shape of the internal wave attractors under the presence of various perturbations. Geometrical ray tracing is used to predict the position of the attractors and further investigate their features. It is found to have a good predictive power. The experiments performed consist of three sets: we start by changing the forcing frequency and we find all the possible shapes of the attractors. Then we perturb the linear stratification of the fluid with a more strongly stratified middle layer and we find that the internal wave attractors persist and that their branches are curved. Lastly we change the shape of the basin by inserting a corrugated sawtooth sidewall. The attractor branches split up but the attractor is still visible and present. The relative length scales of the attractor and the sawtooth are found to determine the extent of the attractor's spatial deformation and the skewness of the wavenumber spectra. We employ the Hilbert transform method to perform directional decomposition of the signal and we find that backscaterring at the sawtooth is significant and it introduces an anticlockwise propagation direction. Even when the basin is highly perturbed, the internal wave attractors are found to manifest the response of the fluid.

Chapter 1

Introduction

Fluids can be stratified due to spatial changes in temperature and/or composition; in addition rotating fluids can be stratified due to changes in angular momentum. In the ocean significant changes in density are observed in the vertical, that is the direction parallel to gravity. A density stratification allows for oscillations of the fluid that have their maximum displacement inside the fluid. The restoring force that is associated with these oscillations is the buoyancy force and the wave phenomena associated are called internal gravity waves. In a continuous stratification these waves have the special property of travelling obliquely into the fluid, maintaining their propagation angle with respect to the vertical. When these waves are present in a confined area they can create spatial patterns called internal wave attractors (Maas & Lam 1995; Maas et al. 1997). The internal wave attractors are closed paths on which the internal wave energy is focused as it propagates and reflects against the walls of the basin. Internal wave attractors, as found in a two-dimensional smooth trapezoidal basin with a linear stratification, have been studied theoretically (Maas & Lam 1995; Lam & Maas 2008), numerically (Grisouard et al. 2009; Hazewinkel et al. 2009) and experimentally (Maas et al. 1997; Lam & Maas 2008; Hazewinkel et al. 2008). Here, we present an experimental study on internal wave attractors where we perturb the smoothness of the basin and the linear stratification.

1.1 Internal waves

Internal gravity waves are quite common in geophysical fluids and are very different from the classical waves encountered e.g. at the surface of the sea, or from acoustic and electromagnetic waves (Maas 2005). Their peculiarity lies in the character of their dispersion relation, which does not prescribe the wavelength but the direction of propagation of the wave. In this section we will present in short the theoretical derivation of the dispersion relation and we will discuss its consequences on the propagation of internal gravity waves. We will also make a short reference to the type of internal waves present in a rotating fluid: the inertial waves.

1.1.1 Internal gravity waves

The vertical displacement of a fluid parcel by some external force in a stratified fluid is counteracted by the buoyancy force. Due to the parcel's inertia it overshoots the equilibrium position resulting in an oscillation. When a periodic forcing is applied, an internal gravity wave is formed that propagates obliquely within the continuously stratified fluid.

Chapter 1: Introduction

In a stratified two-dimensional fluid the spatial part of internal waves, within the linear approximation, satisfies the following hyperbolic partial differential equation (e.g. LeBlond & Mysak 1978) :

$$\frac{\partial^2 \psi_0}{\partial z^2} - \frac{(N^2 - \omega^2)}{\omega^2} \frac{\partial^2 \psi_0}{\partial x^2} = 0, \tag{1.1}$$

which for $\omega^2 < N^2$ is a wave equation, where ω is the frequency of the wave and N, the Brunt-Vaisala or buoyancy frequency. N is a measure of the background density stratification and it is proportional to the square root of the change in density, $\rho = \rho_0 + \rho^*(z)$, with depth :

$$N^2 = -\frac{g}{\rho_0} \frac{d\rho^*}{dz}.$$

By assuming plane wave solutions of the form:

$$\psi_0(x, z) = A e^{i(kx + mz)},$$

where A is the amplitude, and k, m are the wave numbers in the x, z direction respectively, the following dispersion relation is obtained:

$$\omega^2 = N^2 \frac{k^2}{k^2 + m^2} = N^2 \frac{k^2}{\kappa^2} \rightarrow$$

$$\omega^2 = N^2 \cos^2 \theta. \tag{1.2}$$

Here θ is the angle between the wave number vector, $\boldsymbol{k} = (k, m)$, and the horizontal and κ is the wave number magnitude: $\kappa = \sqrt{k^2 + m^2}$. This dispersion relation dictates that waves of a certain frequency, ω, (so-called monoclinical, single-angled, waves (Maas 2005)), will propagate at a fixed angle (θ) in the fluid. The wave energy propagates obliquely downwards or upwards, parallel to the wave crests and troughs. This means that the group speed, $\boldsymbol{c_g}$, is perpendicular to the phase speed, $\boldsymbol{c_p}$, i.e. $\boldsymbol{c_g} \cdot \boldsymbol{c_p} = \boldsymbol{0}$, (see figure 1.1).

Contrary to surface waves, the dispersion relation of internal waves (1.2) does not prescribe a wavelength to a certain frequency. This implies that a single frequency disturbance is not associated with unique wave number components but it generates groups of waves. The dispersion relation (1.2) prescribes the direction of propagation of these waves, that is the direction of the wave number. A consequence of the imposed angle of propagation by the dispersion relation is that upon reflection on boundaries the internal waves must propagate with the same angle with respect to the vertical as that of the incident waves. That is because the frequency remains the same. This means that the angle of propagation of the reflected internal wave is independent of the slope of the boundary and depends solely on the frequency of the incident wave (see fig 1.2). This property is quite unlike that of common waves, for example light reflecting from a mirror, where the angle of incidence also equals that of reflection but with both angles being defined with respect to the normal to the scattering surface. This unique characteristic allows for internal waves to get focused (decrease of wavelength) or defocused (increase of wavelength) when they are reflected from an inclined boundary. When internal waves are focused the energy is also focused. When the
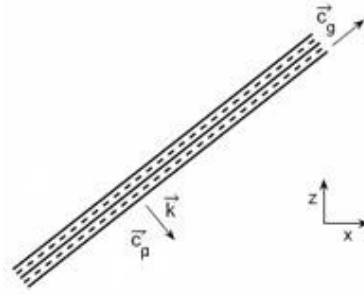
*Figure 1.1 Properties of an internal-wave depicted schematically. The dashed and solid diagonals denote lines of constant phase; they propagate in the direction of the wave number vector, **k**, which in this example points right- and downward. The energy, on the other hand, propagates in the direction of the group velocity vector,c_g, which is perpendicular to c_p. (From Gerkema & Zimmerman, 2008)*

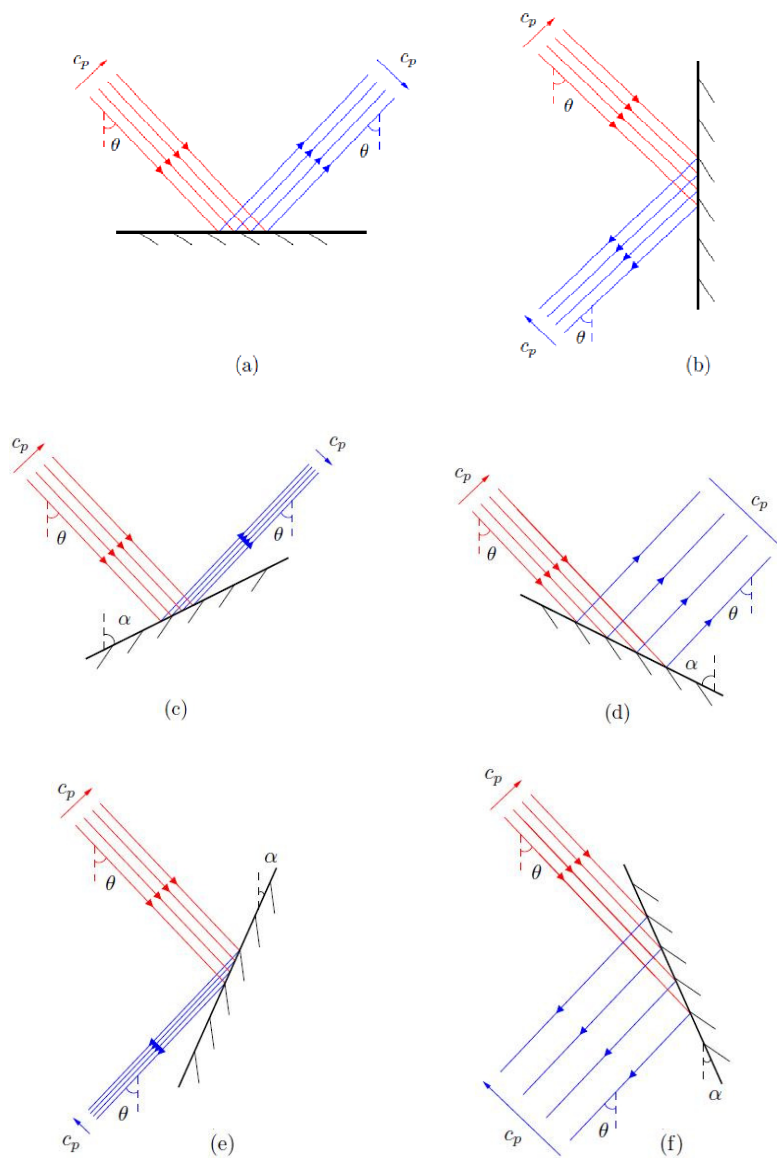*Figure 1.2 Schematic of wave beams reflecting at (a) a horizontal boundary, (b) a vertical boundary, (c) and (d) a subcritical boundary, (e) and (f) a supercritical boundary. Red and blue lines denote the lines of constant phase associated with incident and reflected wave beams respectively. Arrows positioned on phase lines indicate the directions of energy propagation. (Adapted from Nye, 2009).*

angle of the inclined boundary with the vertical is smaller than the angle of propagation of the internal waves the reflection is called supercritical; the reverse case is called subcritical. In both cases the waves can either get focused or defocused upon reflection as depicted in detail in figure 1.2. All the experiments in this thesis are in the supercritical regime.

When an internal wave beam reflects at a piece-wise linear topography, such as the sawtooth (see figure 3.2), backscattering may take place (Nye 2009). A backscattered wave beam propagates along the direction of the incident wave. In some of our experiments we use a sawtooth boundary and we study the role it plays to the focusing of the waves.

1.1.2   Inertial waves

Internal waves can also arise in a rotating fluid that is stratified in terms of angular momentum, even if a density stratification is absent. The restoring force associated with these waves is the Coriolis force (Tolstoy 1973). The ocean, because of the earth rotation (characterized by rotation vector Ω), is stratified in terms of angular momentum. For a solid body rotation this stratification is stable. It is therefore able to support internal waves, termed inertial (or gyroscopic) waves. These waves follow a dispersion relation similar to (1.2) that relates the wave frequency to the angle of propagation and they have the same properties as the internal gravity waves.

1.2   Internal wave attractors

The focusing (defocusing) property of reflecting internal waves allows for the formation of wave attractors when the waves are present in a confined area. Maas & Lam (1995) showed theoretically that in a confined geometry with at least one sloping wall, focusing dominates over defocusing. In such a geometry the waves, following a series of reflections, are attracted to a certain path, they approach a limiting orbit. This closed path is the internal wave attractor.

In a two-dimensional trapezoidal domain with one sloping wall, as depicted in figure 1.3, within certain ranges of frequencies, attractors can arise, whose shape is similar, e.g. trapezoidal as in the example of figure 1.3. The waves are focused on the attractor and so does the energy that travels along the closed path. The wavelength decreases upon each reflection while the amplitude of the velocity increases, implying large shear along the path. When internal wave attractors are present in a basin they set the spatial distribution of energy.

1.2.1   Internal wave attractors in the laboratory

Internal wave attractors in nearly two-dimensional basins have been observed in the laboratory. Although the basins had a finite width, the wave motion was assumed to be uniform in the third dimension (Maas et al. 1997; Hazewinkel et al. 2008). Maas et al. (1997) found experimental evidence of an internal wave attractor, in a trapezoidal tank with one sloping wall. The basin was filled with a linearly stratified fluid and was brought into a vertical oscillation. Initially, wave motions with half the forcing frequency were excited by parametric instability (Benielli & Sommeria 1998). After a certain time and with the process of focussing, the wave motions were finally found to be localized around a closed path in the tank, the attractor, as predicted by theory (see figure 1.4)
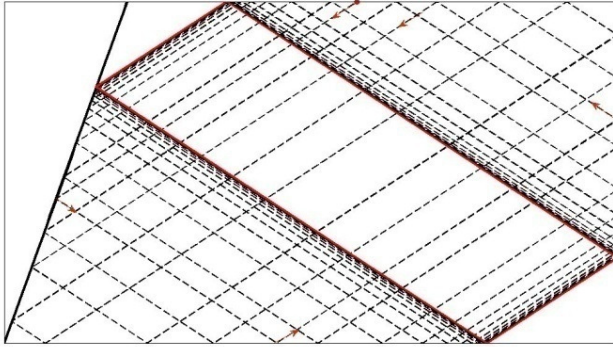
Figure 1.3 Internal wave rays, starting from a red dot at the surface, converge to an attractor in a 2-D trapezoidal geometry with a sloping wall. The dashed lines show the consecutive reflection path of the waves until they reach the red line (internal wave attractor). The arrows indicate the initial anti-clockwise direction of the rays that then changes into clockwise, which is the ultimate focusing direction.
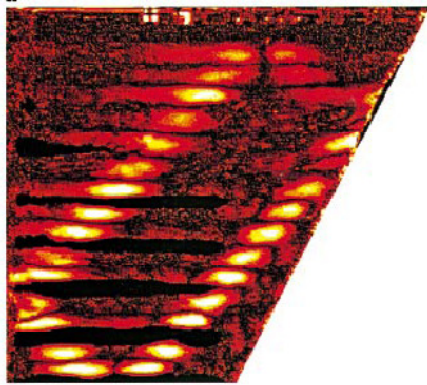

Figure 1.4 Internal wave attractor in a 2D trapezoidal basin. Visualization of the isopycnal displacements (larger in the light areas) was possible with dye lines. Picture taken from Maas et, 1997.

Hazewinkel et al. (2008) performed a series of laboratory experiments to further investigate the dynamics of internal wave attractors in a trapezoidal basin. They studied the development, steady state and decay of an internal wave attractor (fig 1.5). They generated internal waves by vertically oscillating the basin; the basin scale waves reflecting on the sloping boundary were focused on an attractor. After a certain time a steady state was reached and the scale of the attractor was set. They found that the focusing of the basin scale internal waves takes the energy to smaller scales where viscous dissipation dominates preventing any further focusing. When the forcing was terminated and internal waves were no longer generated, the attractor started to decay with the low wave numbers (large wavelengths) disappearing first, as the transfer of energy continued. The disappearance of the low wave numbers showed up as more and more fine structure of the attractor in time. Spectral analysis, (figure 1.6(b)), pointed out that the dominant wave number increases as the attractor decays.

The study of the wave number spectra of the attractor during the steady phase, showed that while following their path around the attractor, starting from the sloping wall and moving clockwise, the high wave numbers disappear and the low wave numbers remain. This viscous broadening of the attractor branches (S1 to S4) corresponded to the shift to lower dominant wave numbers (fig 1.6 - a).
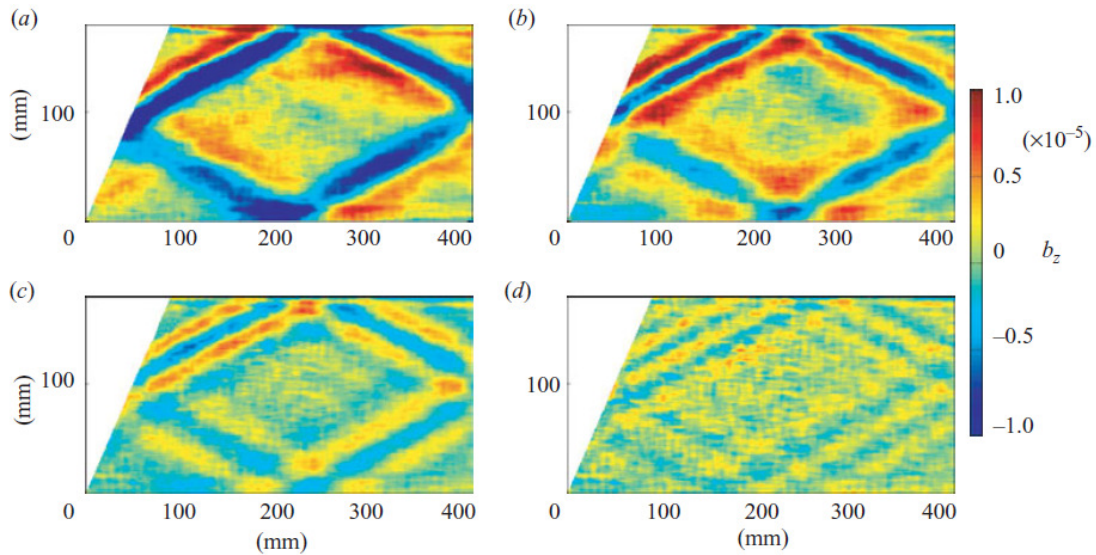
Figure 1.5 Four snapshots of the harmonically analysed density gradient perturbation field, showing the attractor at the steady state (part a) and its decay with time after the forcing was terminated (parts b, c and d) revealing that the shorter wavelengths decay later. (Figures taken from Hazewinkel et al. 2008)
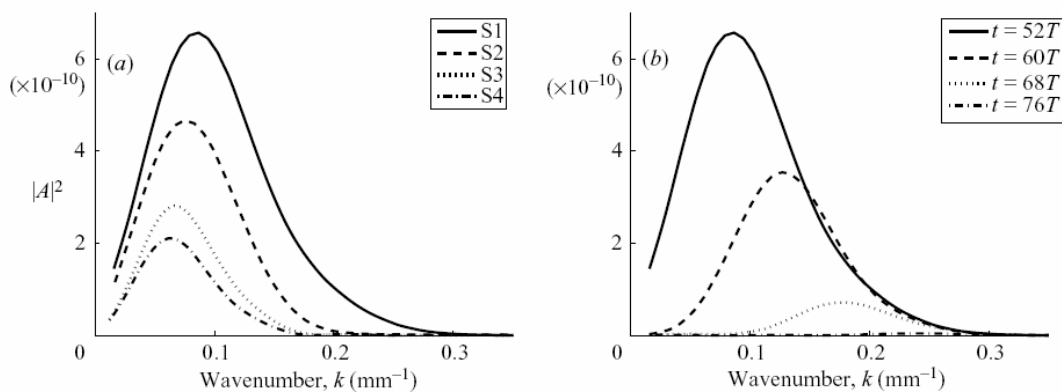

Figure 1.6 Spectral analysis (a) Spectra of harmonic analysis during the first period of the decay. The annotations S1-S4 are related to the four branches, starting from the slope in a clockwise direction; their exact definition will be given in chapter 4. (b) Time evolution of the spectrum along the first branch during the decay phase of the attractor. (Figure taken from Hazewinkel et al. 2008)

1.2.2   Numerical modelling of internal wave attractors

Internal wave attractors were recently modelled numerically by Grisouard et al. (2008) and Hazewinkel et al. (2009) with the MIT general circulation model (Marshall et al. 1997). The laboratory experiment performed by Hazewinkel et al. (2008), described in the previous section, was reproduced with the MIT model in a two-dimensional setting and was compared with the experimental results. Hazewinkel et al. (2009), made a quantitative comparison between the model simulation and the laboratory experiment and they found a strong correspondence. They demonstrated that the numerical model reproduces quantitatively comparable attractors to the laboratory experiments, suggesting that the narrow three dimensional tank can indeed be considered effectively two dimensional.

6

1.3 Relevance of this research

The experimental research on two-dimensional internal wave attractors performed to this date focuses on the simple case of a trapezoidal basin with smooth sidewalls and uniform stratification. Within this setting the forcing frequencies used are chosen such that only the simplest of all attractors is found (van Breevoort, 2007). The next step toward a holistic representation of the two-dimensional internal wave attractors is to investigate whether they are also found when perturbations to the basin shape or to the linear stratification are made, or when the forcing frequency is varied. This comprises the topic of this thesis.

We investigate the perturbed internal wave attractors with a series of experiments performed in a two-dimensional trapezoidal basin similar to the one used by Hazewinkel et al. (2008) and we study the occurrence and position of the attractors using the ray tracing method (Maas & Lam 1995). We start by scanning the smooth basin filled with linearly stratified fluid with various forcing frequencies. We show that complex internal wave attractors can be formed whose structure is predicted by the ray tracing method. Then we fill the tank with fluid having a non-uniform, three layer type of stratification, in which the rate with which density increases, varies with depth. We observe transmission and reflection of the generated internal wave beams at the interfaces of the layers but we find that an internal wave attractor still exists in such a setting and consists of curved rays. Finally, the tank is filled again with linearly stratified fluid and we perturb the shape of the vertical side wall of the basin with a variety of sawtooth corrugations. As mentioned in section 1.1, when an internal wave beam reflects on a piece-wise linear topography, such as a sawtooth wall, backscattering takes place. We observe this in the tank and we find that the attractor shape becomes complicated but it is not removed. The ray tracing method was adapted for the perturbed side wall and it approximately gives the shape and location of our observations. This setting is further explored with ray tracing and we find that the corrugations can radically change the geometry of the tank affecting the occurrence of internal wave attractors.

With the work presented here, the complexity level in the study of two dimensional internal wave attractors is raised. The importance of the internal wave attractors in setting the spatial energy pattern when present in an enclosed domain is stressed. The internal wave attractors are found to manifest the fluid response even when the basin is highly perturbed. Moreover the ray tracing method was found to have a good predictive power, regardless of its simple nature, when its limitations are taken into account.

1.4 Thesis outline

The thesis is organised as following: In chapter two we present the ray tracing method first used by Maas & Lam (1995) for smooth basins and we adapt it to the perturbed basin shapes by introducing a sawtooth boundary. Through a number of examples we show the effect of the corrugations on the attractors. In chapter three we present the set up of the laboratory experiments and describe the visualisation techniques used (synthetic schlieren, Dalziel et al. 2000; Hilbert transform, Mercier et al. 2008). In chapter four the default experiment is described. This experiment was performed in a smooth trapezoidal basin filled with linear stratification and it is used as a reference point for the perturbed variations following in chapter five. There, the three sets of experiments performed are presented: the frequency scan, the non-uniform stratification and the sawtooth topography. We end up with a summary of the conclusions in chapter six.

Chapter 2

Ray tracing in an enclosed domain

In this chapter we describe the ray tracing model used to predict the type and position of internal wave attractors for the laboratory experiments performed. The ray tracing technique applied to internal waves attractors was originally used by Maas & Lam, 1995 for a number of smooth basins assuming linear stratification. Here, we use this method to scan the basin for a series of frequencies and we expand it to include a corrugated sidewall.

2.1 Ray tracing model

Internal waves can be described in terms of rays. The rays are straight lines, parallel to the lines of equal phase, showing the energy propagation. They make a fixed angle with the vertical, determined by the dispersion relation (eq. 1.2):

$$\theta = \arccos\left(\frac{\omega}{N}\right).$$

The rays coincide with the characteristics of the hyperbolic partial differential wave equation of internal waves (eq. 1.1). The characteristics are lines on which a partial differential equation has the same solution. This amplifies the importance of rays in the internal wave application. They can be used to construct exact solutions geometrically.

Ray tracing is commonly used in linear geometrical optics to describe the behaviour of wave characteristics (e.g. Lighthill 1978). Longuet-Higgins (1969) showed the scattering behaviour of internal waves using the geometrical ray tracing method and Maas & Lam (1995) used ray tracing to describe the geometric focusing of internal waves in an enclosed basin. Following a ray that starts from a point at the surface of the fluid we can trace its path in an enclosed domain. The ray bounces at the boundaries like a frictionless ball on a billiard table (Maas & Lam, 1995) but with a major difference: when it hits an inclined boundary the angle of the reflected ray does not equal the angle of incidence relative to the bottom normal, see figure 1.2. The angle of propagation for a certain stratification and frequency does not change and the ray (energy) is permitted to move only in one of the four directions defined by θ. By following a simple iterative bouncing process we can predict the existence and position of an internal wave attractor in a two-dimensional domain.

We followed this procedure to model the internal wave attractors expected to be found at the laboratory experiments. In the model we introduce a system of stretched non-dimensional

coordinates following Maas & Lam (1995). By combining the frequency, ω, and the stratification, N, to the depth, H, and basin half-width, L, we define the dimensionless depth, τ. In a trapezoidal domain, this is:

$$\tau = \tan\theta \frac{H}{L} = \left(\frac{N^2}{\omega^2} - 1\right)^{1/2} \frac{H}{L}. \tag{2.1}$$

The horizontal coordinate, x, is scaled with half width, L, so the centre of the tank is 0 and the value of this coordinate can vary from −1 to +1. The intersection point of the slope with the top of the tank is defined as $x = d$; for $d = -1$ the tank has a rectangular shape and for $d = +1$ the tank has a triangular shape. By using this scaling the characteristics have a fixed angle of 45° with the vertical.

The rays can start from any given point of the surface but for the same forcing frequency and stratification in a smooth 2-d trapezoidal basin, all converge onto the same internal wave attractor,. The direction that a ray initially moves, that is to the right or to the left, does not influence the uniqueness of the attractor. An example where from two points at the surface the rays are followed for 1000 iterations, coloured red and blue, is given in figure 2.1. Both of them converge to the same rectangle, the internal wave attractor. In this example the parameters used are $\tau = 1.66$ and $d = -0.43$. The value of d corresponds to the trapezoidal basin filled at $H = 260\ mm$, used for the default experiment.

2.2 Frequency scan with the ray tracing model

When the forcing frequency changes the angle of propagation of the waves changes according to the dispersion relation and a different internal wave attractor is formed. In the ray tracing model, instead of changing the angle of propagation of the rays we adapt the tank dimensionless depth (τ). For example two different forcing frequencies, $\omega_1 = 1.46\ rad\ s^{-1}$ and $\omega_2 = 1.78\ rad\ s^{-1}$, in the same tank filled with water of the same stratification ($N = 2.15\ rad\ s^{-1}$) and the same height, will result in two different internal wave attractors, as shown in figure 2.2, with $\tau_1 = 1.49$ and $\tau_2 = 0.94$ (here plotted in the original, fixed basin shape).

The periodicity of an attractor is defined by two numbers (a,b), indicating the times it reflects on the surface, (a), and on the side boundaries, (b), accordingly; for example the attractor for $\tau_1 = 1.49$ of figure 2.2 is a (1,1) attractor indicating one reflection at the surface and one on each sidewall. Accordingly, the attractor for $\tau_2 = 0.94$ is a (2,1) attractor.

By scanning the basin with a range of frequencies the occurrence of attractors can be found for a certain basin and stratification. We do this with the ray tracing model by varying τ. In the following bird eye view τ-x diagram (figure 2.3) the reflections of the characteristics on the surface are shown, between 950 and 1000 iterations, for a range of τ from 0.8 to 2.1. Within this iterative range the x-positions are indicative of the points that an attractor reflects at the surface. For our tank, ($d = 0.32$ and $N = 2.15\ rads^{-1}$), the τ range corresponds to a forcing period range of $3.41\ s$ to $5.28\ s$. In the diagram the areas of the (1,1) and (2,1) attractors are clearly visible. In the experiments described in chapter 5, a frequency scan of the basin will be done within the period range shown in the diagram and the different kind of attractors found will be shown and compared with the results of the ray tracing model.
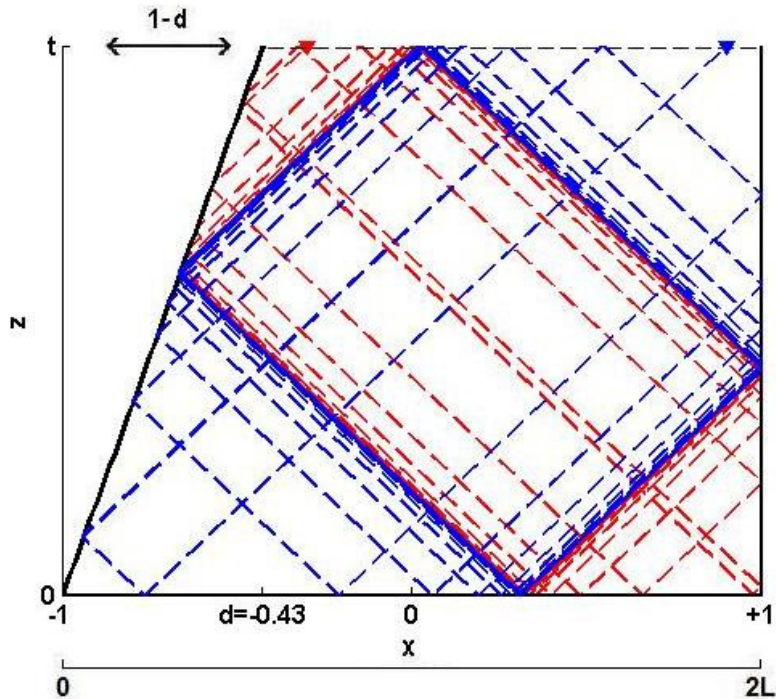
Figure 2.1 Ray tracing of internal waves in an enclosed 2-d trapezoidal basin with $\tau = 1.66$ and $d = -0.43$. The red dotted line depicts the path of a ray starting leftwards at the surface at $x = -0.3$ and the blue one a ray starting from $x = 0.9$, see triangles. They both converge on the same internal wave attractor.
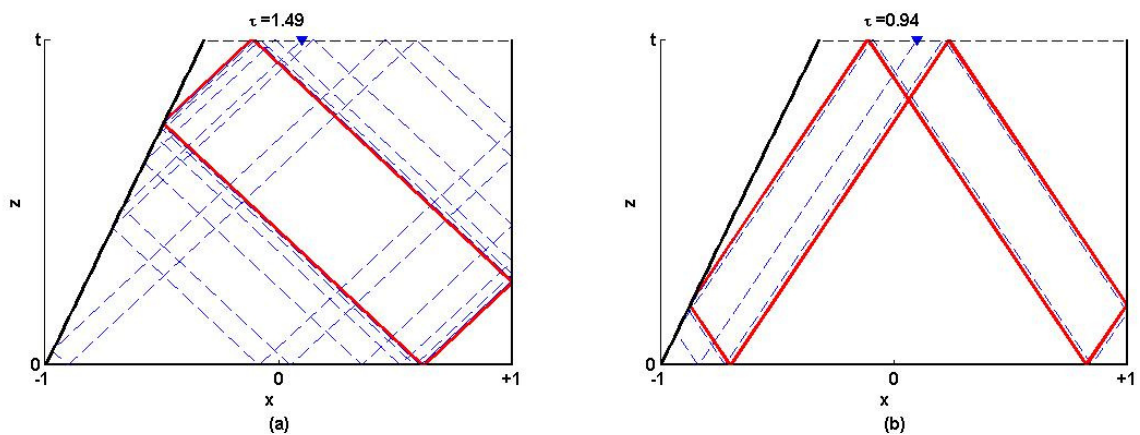

Figure 2.2 Ray tracing of internal waves in an enclosed 2-d trapezoidal basin ($d = -0.32$) with $\tau = 1.49$ and $\tau = 0.94$. The blue dotted line depicts the path of a rays starting at $x = 0.1$ and the red solid line is the focused rays on the internal wave attractor.

2.3 Perturbing the ray tracing model

The ray tracing model presented in the previous paragraphs describes a smooth trapezoidal basin. One of the objectives of this thesis is to study the internal waves attractors in a perturbed environment. For this we introduce a corrugated topographic profile at vertical side-wall of our model and we follow the ray paths. The corrugations used are rectangular triangles (sawtooth) and are characterized by a horizontal length scale, l_c ; the height of the triangle changes with the width. Note that the appearance of the triangles, plotted in this chapter, is affected by the stretched representations of the basins.
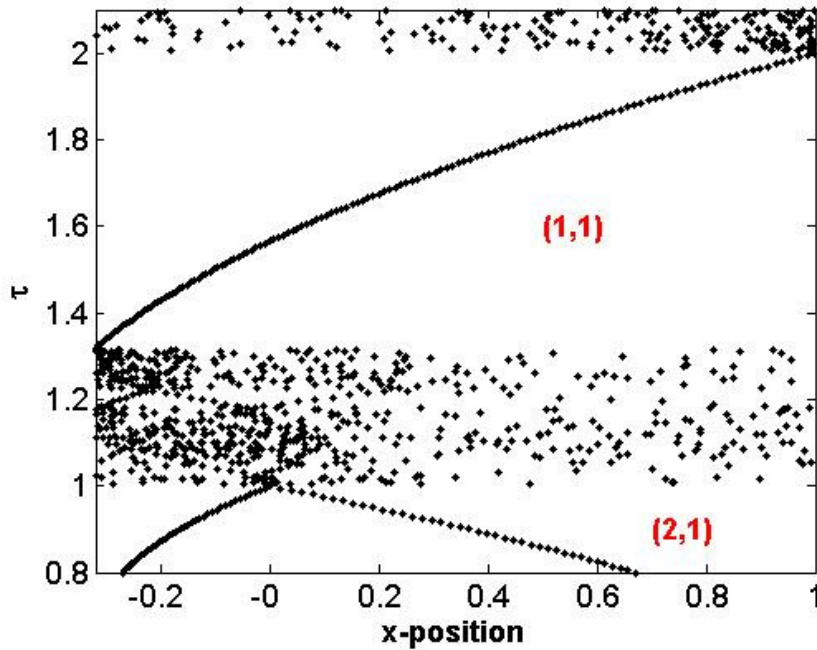
Figure 2.3 Bird eye view of the x-position of an attractor reflecting at the surface shown by following a ray from 950 to 1000 iterations in a basin with $d = -0.32$.

The procedure followed is the same as in the smooth case. We shoot the rays from the surface and follow their path for 1000 iterations. We are going to examine some perturbed basins and we are going to compare the bird eye view diagrams with the smooth case (figure 2.3), in order to detect how the shape and existence of the attractors are affected by the corrugations. We also use this model to simulate the experiments performed with a sawtooth side-wall.

2.3.1 Varying the number of peaks

We vary the number of peaks of the corrugated boundary; we start by introducing only one peak and then we subsequently introduce three, seven and twenty peaks. The position of the attractor is determined by τ and d as before but it may also be affected by the corrugations. For the attractors shown in figure 2.4 the same τ and d were used as in figure 2.2(a), so any difference in their position is due to the presence of the sawtooth boundary. We observe that the larger the corrugation wavelength the bigger the excursion of the focusing loop compared to the attractor of the smooth boundary case. It can well be argued that since the geometry of the tank is changing radically in the presence of the sawtooth, the τ parameter should be redefined. However, we simply use it, as defined in equation 2.1, as a comparative measure of the excursion of the "smooth" attractor due to the corrugations.

2.3.2 Varying τ

Next we are going to vary τ to see how the corrugated walls affect the bird-view τ-x diagram. We are going to zoom into (1,1) attractor region for a varying number of corrugations and compare it with figure 2.3, see figure 2.5. The first point to notice is that an attractor exists for every τ of the (1,1) region of the smooth case, $1.32 \leq \tau \leq 2$. However, the lower limit of this region, $\tau = 1.32$, is expanded as the perturbation of the basin increases. For $n = 2$ peaks, the lower τ limit is $\tau = 1.23$; as the number of corrugations increases, so the perturbation becomes
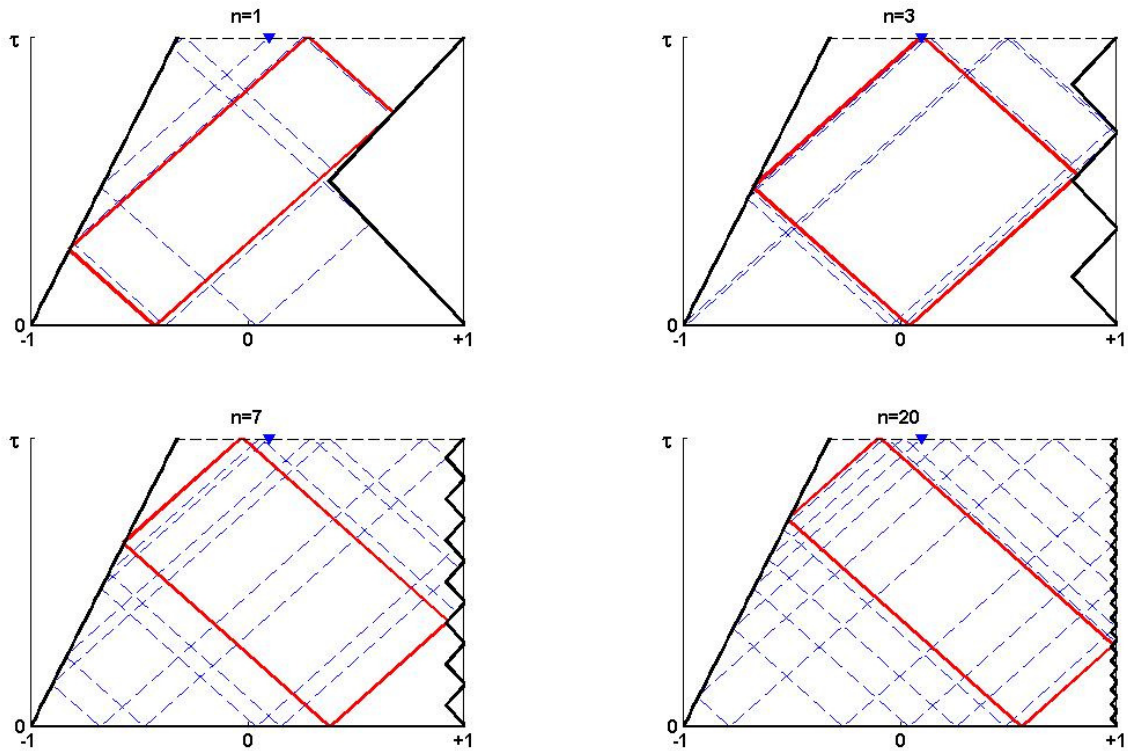
Figure 2.4 An internal wave attractor in a trapezoidal basin with sawtooth sidewalls of varying corrugation numbers, $\tau = 1.49$ and $d = -0.32$. Rays starting at $x = 0.1$. Note that the rectangular triangles from which the corrugations are built, are stretched in these representations. Compare with smooth sidewall case, figure 2.2 (a).
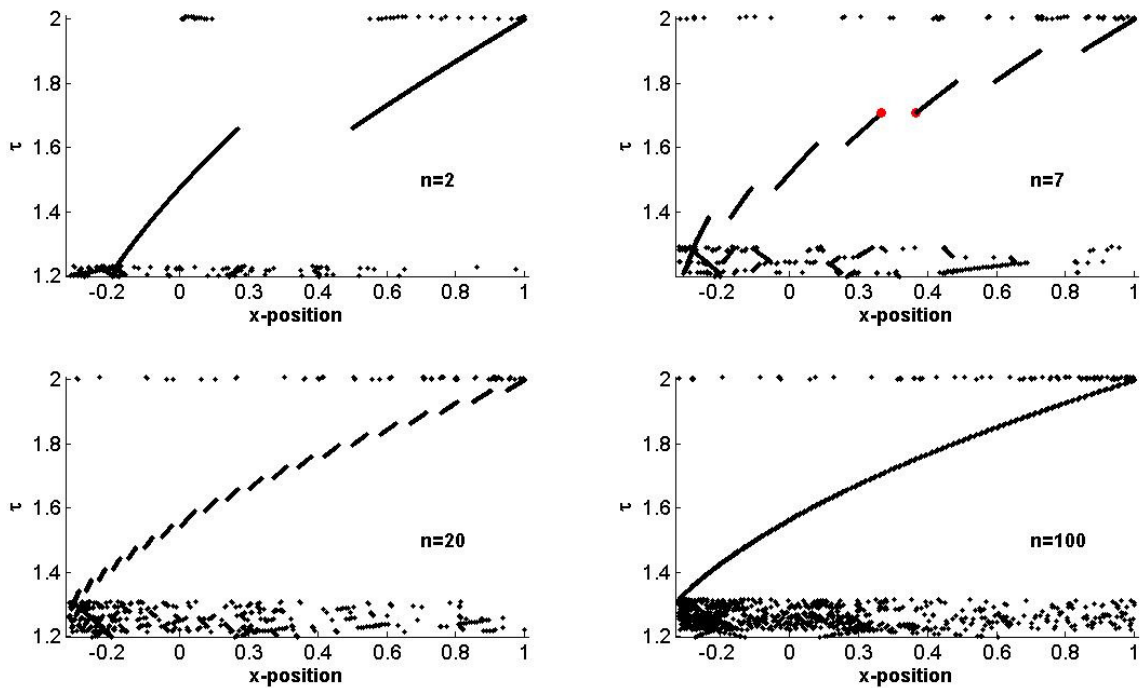

Figure 2.5 Bird eye view of the x-position of an attractor reflecting at the surface shown by following a ray from 1900 to 2000 iterations in a basin with $d = -0.32$ and varying number of corrugation peaks (n). The number of peaks is indicated in each diagram. The two red marks at the n=7 diagram indicate the points considered for figure 2.7.

less significant, the lower τ limit tends to reach the value of the smooth case lower limit, that is $\tau = 1.32$. In general, the appearance of the bird eye view diagram resembles more the smooth boundary case as the number of corrugations increases, and for n=100 it is almost identical.

Obviously, one of the consequences of the corrugations is the appearance of discontinuities on the transition of the x-position of the attractor from the one end of the basin to the other. These jumps are associated to the number of peaks of the corrugated side-wall, n. There appear to be $n - 1$ such jumps. What actually happens to the attractor can be seen in figure 2.6, where we plot the attractor in a $n = 7$ basin and for the values of τ at the discontinuity jump marked with red in figure 2.5. In figure 2.6 we see that the internal wave attractor for $\tau = 1.709$ (exactly after the jump) needs a large number of iterations in order to be established. In the bird eye view diagram discontinuities are visible. The part of the sawtooth sidewall that the rays need to reflect on, for the transition of the surface x-position to be continuous, is locally defocusing the rays. This makes the establishment of an internal wave attractor impossible at the specific position. However, the focusing from the sloping side-wall dominates and the attractor is finally established.
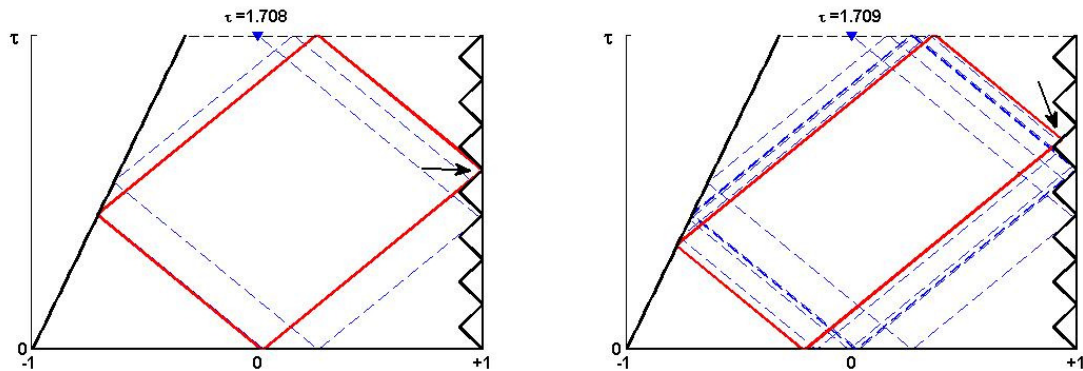

Figure 2.6 An internal wave attractor in a basin with n=7 peaks for two neighbouring values of τ indicated by a red mark in figure 2.6. The ray path to the establishment of the attractor is shown with the thin dashed blue line. The attractor for $\tau = 1.709$ needs a large number of iterations to be established. The thick dashed blue line on the right repeats the attractor shape on the left.

2.3.3   Varying the initial position

Observing the sensitivity of the attractor position to changes in the corrugated geometry, a question that occurs is: Is the attractor occurrence influenced by the initial position that a ray is shot? If this is true then for a certain frequency, contrary to the smooth basin case (figure 2.1), more than one attractors may appear,. Maas & Lam (1995), showed that in a bucket-shaped domain for odd-period attractors, that is attractors that reflect an odd number of times at the surface, as the (1,1) attractors that we examine, there are two separate limit cycles instead of one. Which one is established depends on the surface position and the direction (left or right) that the ray is shot. The presence of only one limit cycle in the smooth case (figure 2.1) is exceptional, owing to the symmetry of the trapezoidal basin.

In figure 2.7 an example is shown that confirms the dependence of the attractor position on the initial shooting point for a corrugated wall with $n = 7$ peaks. When the direction of the ray is to the right, two limit cycles appear (blue and red lines), where if the ray is shot to the
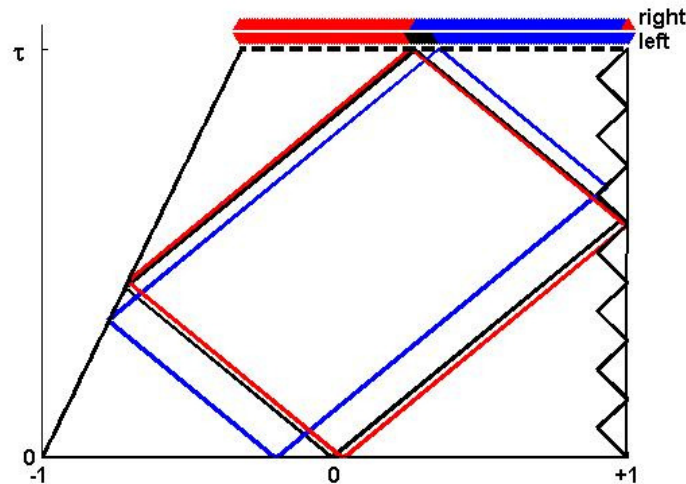
13

Figure 2.7 The dependence of the position of an internal wave attractor on the initial point and direction of shooting a ray in a trapezoidal basin with a sawtooth side-wall $n = 7$ and $t = 1.7$. The attractors plotted are the ray paths between 1900 and 2000 iterations (note that a greater number of iterations results in the same attractors). The red line depicts the focusing loop for rays starting from $-0.32 \leq x \leq 0.27$ and $x = 1$ for right moving rays and from $-0.32 \leq x \leq 0.25$ for left moving rays; the black for rays starting from $0.26 \leq x \leq 0.35$ for left moving rays. and the blue for rays starting from $0.36 \leq x \leq 1$ for left moving rays and from $0.26 \leq x < 1$ for right moving rays. The surface points have been coloured accordingly for the left and for the right moving rays.

left one more limit cycle appears (black line), giving in total three possible cycles. The red attractor appears for right moving rays starting from $-0.32 \leq x \leq 0.27$ and x = 1 and from $-0.32 \leq x \leq 0.25$ for left moving rays; the black attractor appears only for left moving rays starting from $0.26 \leq x \leq 0.35$; and finally the blue attractor appears for left moving rays starting from $0.36 \leq x \leq 1$ and from $0.26 \leq x < 1$ for right moving rays. In a real basin the rays are theoretically emanating from the whole surface, so maybe in the presence of a corrugated sidewall, more than one attractor is visible in one experimental setting.

2.4 Limitations of the ray tracing method

An effect of the corrugated side-wall that ray tracing fails to predict for the subcritical regime, angle ray steeper than angle topography ($\theta < \alpha$), is the backscatter of the wave beams from the corrugations (Nye, 2009). According to the theoretical predictions of Baines (1971) for a sinusoidal boundary, when a wave beam reflects at the topography it is being scattered. Part of its energy is being scattered forward, that is along the direction predicted by ray tracing, and when ($\theta < \alpha$) part of the energy is being scattered backward, propagating along the direction of the incident wave but in the opposite sense. Nye (2009) showed, with experimental observations, that piece-wise linear topographies, including the sawtooth, give a backscatter component, similarly to the sinusoidal boundary. On the contrary, ray tracing does not predict a backscatter component (Longuet-Higgins, 1969). Backscattering, although not predicted by ray tracing is expected to appear in our experiments too. To investigate backscattering, we employ the Hilbert transform method described in chapter three.

Another weakness of the ray tracing method, when used to simulate experiments, is related to its sensitivity to the input parameter τ. As we saw, a small change in τ can result in different focussing loop shapes. According to equation 2.1, τ depends on the stratification, frequency and dimensions of the basin. Thus, small experimental errors may prevent ray

tracing from accurate predictions. The predictive power of ray tracing is tested in chapters 4 and 5, where its outcome is compared with the experimental data.

Chapter 3

Experimental set up

The experiments were performed in the GK Batchelor Laboratory of the University of Cambridge. The set up consisted of a trapezoidal tank similar to the one used by Hazewinkel et al. (2008), a horizontally oscillating platform where the tank was mounted on and a camera for recording. To visualize the internal waves, synthetic schlieren (Dalziel et al., 2000) was used, which gives the perturbation density gradient fields. To study in detail the direction of propagation of the waves the Hilbert transform technique was employed (Mercier et al., 2008).

3.1 Generation of internal waves

3.1.1   The tank

The experiments were performed in a narrow rectangular tank with a sloping end wall fixed at the bottom at an angle, α, of 27° to the vertical and dimensions 330 x 101 x 453 mm (height x width x length). The wave motion in this tank was approximately uniform in the narrow cross tank direction (y), so we can refer to the setting as quasi two dimensional, with the horizontal and vertical coordinates, x and z respectively, being the ones of interest in our study.

To study the response of the internal wave attractors to a perturbed basin, we performed a series of experiments with three different corrugated side walls consisting of rectangular triangles with varying length scale, (figure 3.2). The corrugations were always attached on the vertical side-wall opposite to the sloping wall over the whole width. Each sidewall is characterized by a length scale, l_c, defined as the distance between two subsequent peaks. In table 3.1 the characteristics of the sidewalls are presented.

3.1.2   Filling the tank

The fill the tank, we used two computer-controlled Masterflex peristaltic pumps. Each pump was connected to a basin of water, one filled with water of high salinity and one with fresh water. The flow of the pumps was programmed such that the desired stratification would result. The use of the pumps instead of the double bucket method allows for a linear stratification in a tank in which the horizontal dimension varies with height (Breevoort, 2007). For the experiments involving the non smooth sidewalls and the frequency scan, the tank was
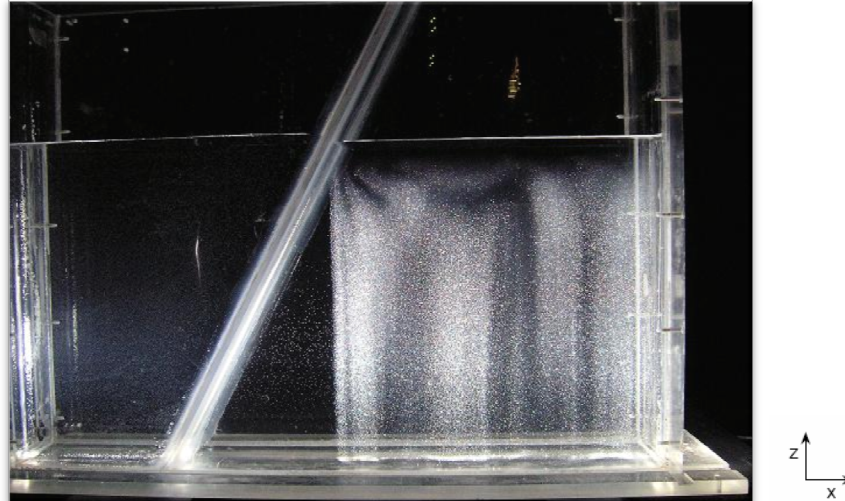
Chapter 3: Experimental set up

Figure 3.1 The tank used for the experiments filled with water and pearlescence particles. Picture taken during a Particle Image Velocimetry experiment.

Name	Shape	Length scale, l_c, (mm)	Nr peaks	Peak angle
P II (Tiny)	Triangular	10	20	90
P III (Small)	Triangular	38	7	90
P IV (Aggressive)	Triangular	74	3	90

Table 3.1 Characteristics of the corrugations attached to the vertical side wall of the tank.
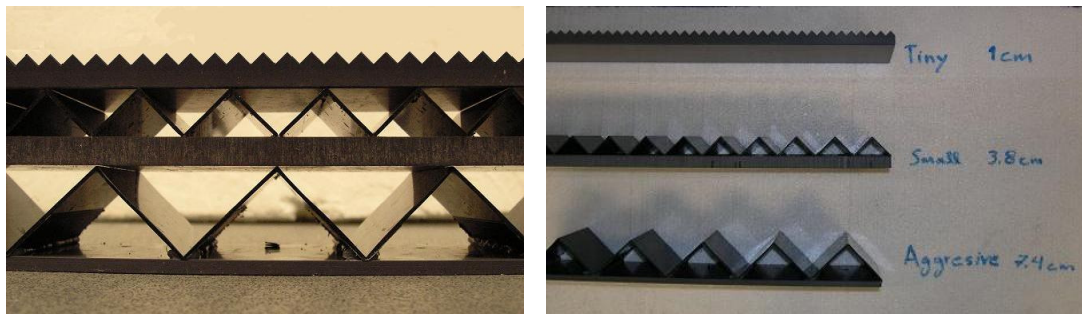
Figure 3.2 The three sawtooth sidewalls used for our experiments.

filled with continuously stratified water of $N \cong 2.2\ rad\ s^{-1}$ and a depth of approximately $280\ mm$. For the experiments with the non uniform stratification, the stratification was characterised by a steeper gradient in the middle. That is: $N = 1.8\ rad\ s^{-1}$ for the bottom layer, $N = 3\ rad\ s^{-1}$ for the middle layer and again $N = 1.8\ rad\ s^{-1}$ for the top layer. The Masterflexpumps were programmed using a hyperbolic secant function:

$$N(z) = N_0 \left(1 + d\ \mathrm{sech}^2 \left(\frac{z - H/2}{L} \right) \right),$$

where $N_0 = 1.8\ rad\ s^{-1}$, $d = 0.7$, $L = 0.5$ and $H = 2.9$. For a graphical representation see fig 3.3.
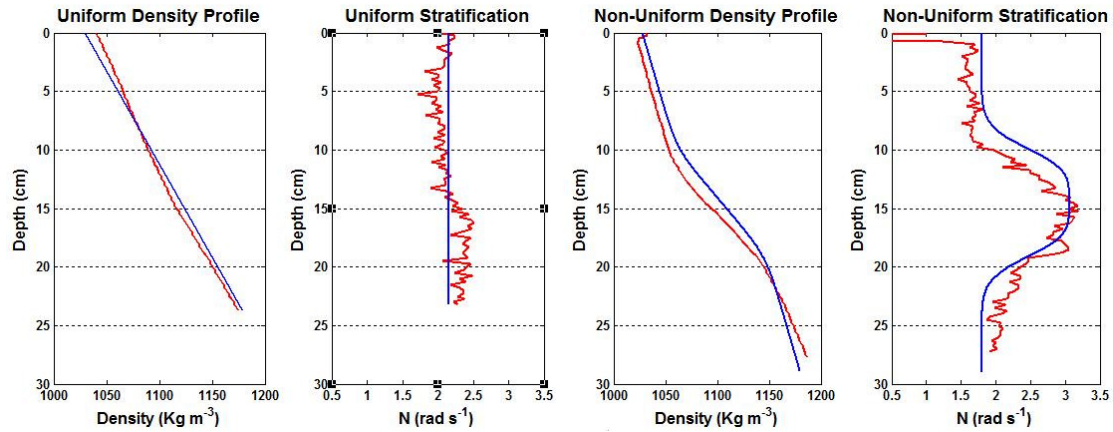
Figure 3.3 Density profile and Brunt-Vaisala frequency for the uniform and non-uniform stratification experiments. The blue line indicates the desired stratification and the red line shows the measured stratification.

To establish the stratification we used a density probe that could traverse the tank. The probe was sampling the water as it moved from the top to the bottom of the tank and an output voltage was given, by measuring the conductivity of the sample. The voltage indication of the probe was calibrated by using water samples the density of which varied from 0.9988 g cm^{-3} to 1.1780 g cm^{-3}; these were the minimum and maximum density values used in the experiments. For the calibration of the density probe we had to take into account the following: firstly, the density of the water depends also on the temperature and secondly, the voltage output of the probe is correlated to the conductivity of the water which in turn depends on the temperature in a way that is dictated by the density. For the range of salinities that we used, a change of 5^{0}C in the temperature changes the density in the order of 10^{-3}, which is negligible, so we assume the density to be constant with temperature. However, the dependence of the conductivity on the temperature cannot be neglected. At high salinities the response of the probe varied significantly with temperature (see fig 3.4). Measurements up to 6 V, indicating low salinities up to 1.1 g cm^{-3}, were quite consistent with temperature and introduced errors only at the third decimal point of the density. Measurements higher than 6V, salinities higher than 1.1 g cm^{-3}, had a certain degree of uncertainty since they could introduce errors at the second decimal point of the density. For this reason, for every density measurement with the probe we also measured the average temperature of the water in the tank and we used the appropriate calibration curve to get the density values. We refer to the average temperature as the top and bottom of the tank had about 1 ^{0}C difference.

3.1.3   Oscillation on the platform

The internal waves were forced by horizontally oscillating the tank. The sloshing on the sloping side of the tank created basin scale internal waves that focus with subsequent reflections. To achieve the oscillation, the tank was placed on a horizontally, nearly sinusoidally, oscillating platform driven by a rotating wheel mechanism (fig 3.5) with an adjustable amplitude. The frequency and the amplitude of the oscillation were controlled.

The frequency was set by a remote external control which was calibrated before the experiments started. To calibrate the frequency control we performed a series of measurements for all the possible values. The indications on the control and the
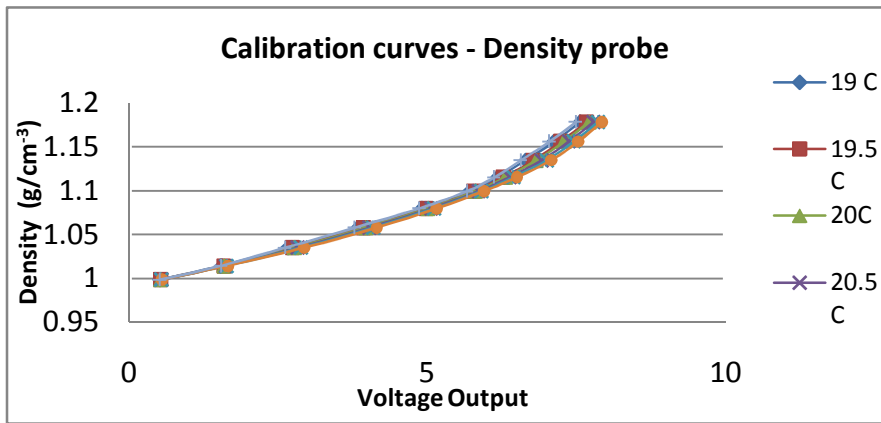
Figure 3.4 Calibration curves of the density probe indicating the varying response of the probe output (voltage) to different temperatures.
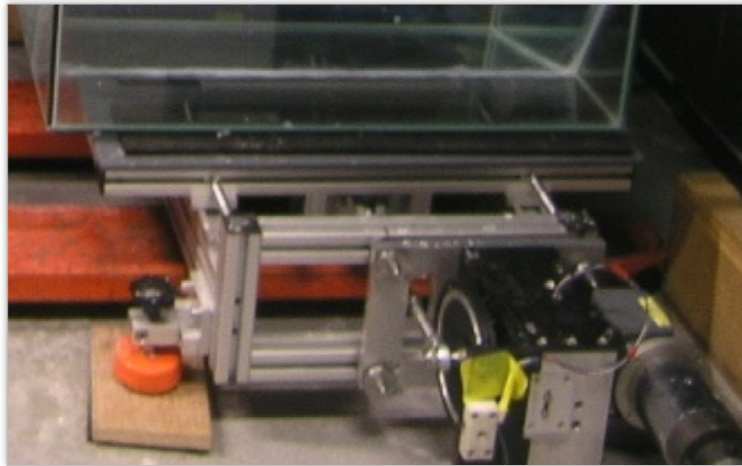

Figure 3.5 The platform supporting the tanks. The rotating wheel giving motion to the platform is visible in the right bottom corner.
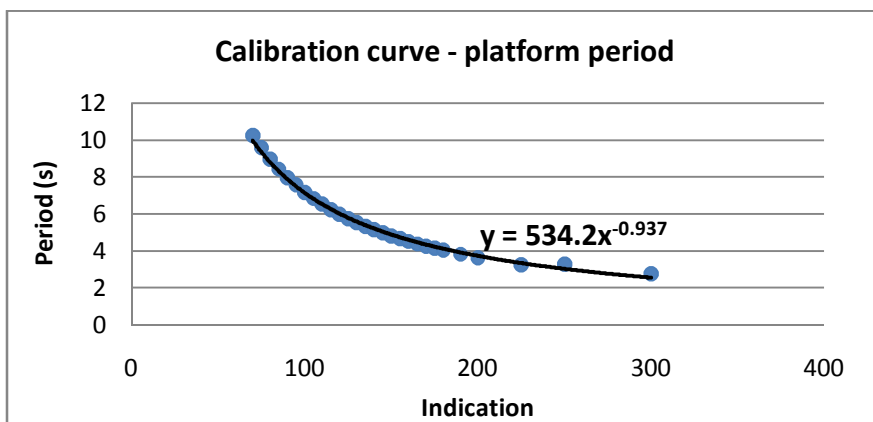

Figure 3.6 Calibration curve for forcing period of the platform.
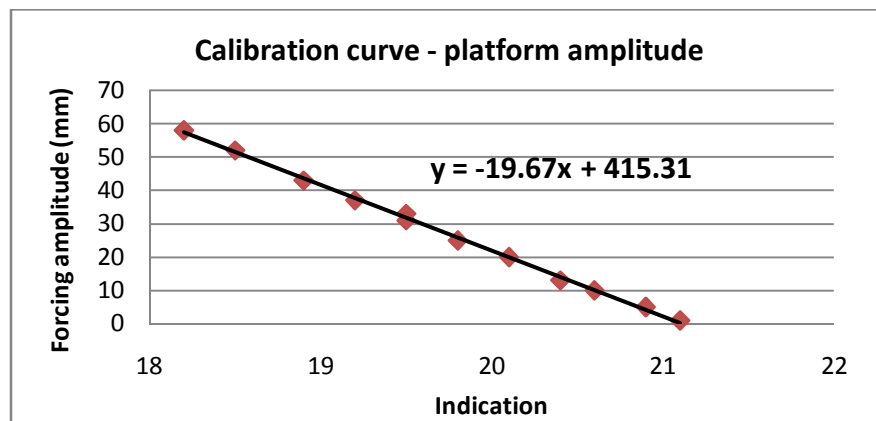
Figure 3.7 Calibration curve for the forcing amplitude of the platform.

corresponding oscillation periods are shown in figure 3.6. The wave motions generated with this method have a frequency equal to the forcing frequency. For the experiments presented here, the amplitude of the platform oscillation was set to 2 cm by setting the radius of the adjustment point of the motor wheel of the table. The calibration curve, $y = -19.67x + 415.31$, is shown in figure 3.7.

3.2 Observing the Internal Waves

3.2.1 The synthetic schlieren method

To measure the motions in the fluid the synthetic schlieren method was used. Synthetic schlieren, introduced by Dalziel et al. (2000), allows for a fine study of the density differences in a fluid. This is achieved by measuring the refractive index changes resulting from density perturbations and comparing them to an unperturbed image. When a light ray passes through the fluid, the direction of propagation of this ray is altered according to the local value of the gradient of the refractive index. The density perturbations change the refractive index, hence change the direction of the light. This is observed as apparent movement of a fixed random dotted pattern placed on a light-bank behind the platform. So by measuring the apparent displacements of the dots we can deduce the density perturbations, $\rho'(x,t)$, by comparing with an unperturbed reference image.

3.2.2 The laboratory set up

For our experiments a random dot pattern (fig. 3.8) was attached to a light bank placed in a fixed position of about 0.5 m behind the oscillating platform and the tank. The apparent movement of the dots was captured by a Jai CV-M4+CL camera (1.3 M Pixel Monochrome) which was placed on the opposite side of the light bank at a distance of about 8m from the tank; at this distance the rays reaching the camera were approximately parallel. The camera was connected to the laboratory computer, where the frames captured were translated into perturbations of the density gradient and stored.

For the part of the experiments that the tank was oscillating, the camera was phase locked with the oscillation, capturing an even number of frames evenly spaced through each forcing period. For most of the experiments 16 frames per period were captured. The signal to capture an image was given by an optical eye which monitored a number of triggers (screws)
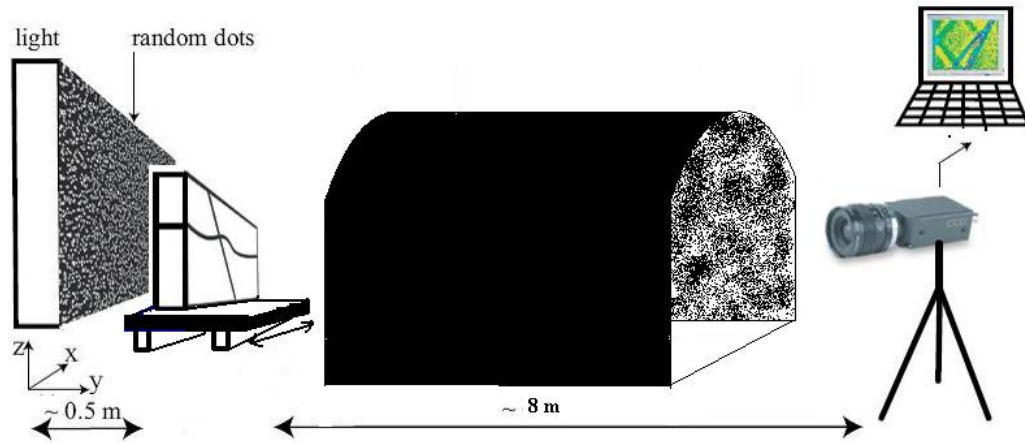
Figure 3.8 Experimental set-up

placed on the driving rotating wheel of the table. The time interval between capturing the images was constant (since the revolution period is constant) so we had an image of the tank at exactly the same spot, for 16 spots. This enabled us to further analyze the data, with each of the 16 snapshots having each their own (unperturbed) reference frame.

Fluctuations of the temperature between the tank and the camera result in a change of the refractive index of the air. Because the synthetic schlieren method is very sensitive, a slight breeze in the lab or even the presence of a person close to the set up can be recorded by the camera. In order to minimize the contamination of the air motion, a tunnel of $8\,m$ long was set up, to isolate the space between the tank and the camera.

3.2.3   Gradient fields and Digiflow

The analysis of the captured images was done with Digiflow (Dalziel Research Partners, Cambridge), a software package able to compute the density gradient variations. Digiflow compares the captured images with a reference unperturbed image, taken before the tank starts moving and it uses the non-dimensional quantity:

$$b = (b_x, b_z) = \nabla\rho' / (\partial\rho^*(z)/\partial z),$$

which is the perturbation density gradient relative to the density gradient of the unperturbed background stratification. These quantities can be understood if we take a look at Fig. 3.9 originally presented by van Breevoort (2007). In this illustration, pycnoclines (solid), perturbed from the background stratification by an internal wave (along the red dashed line) are plotted. By following the arrows, one observes gradients in the perturbation density, with respect to the background stratification, in both directions, i.e. the perturbation heights of the pycnoclines change along the arrows.

In a strong stratification the density perturbations give rise to stronger changes in the refractive index. As a result the dots appear to move for much smaller perturbations. For this reason we aimed at filling the tanks with highly stratified water, $N > 2\,rad\,s^{-1}$. In our analysis we present the horizontal component of the perturbation gradient density field b_x.
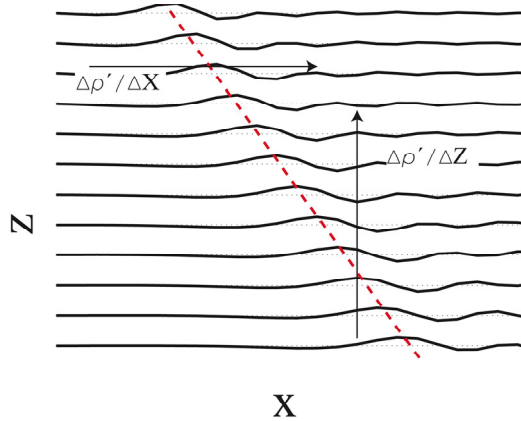
Figure 3.9 Qualitative illustration of b_x and b_z. The solid black lines indicate the pycnoclines perturbed by an internal wave (red line). If the arrows are followed, a gradient in the perturbation height (thus density) is observed in the x- and z-directions.(Figure taken from van Breevoort, 2007)
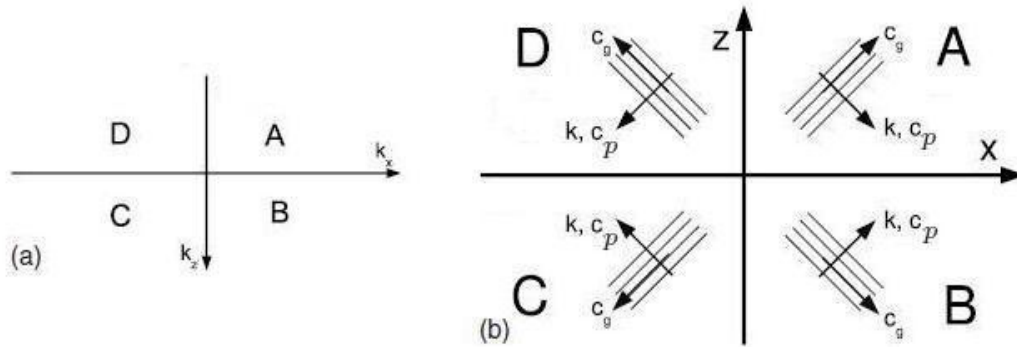

Figure 3.10 (a) Fourier space. The four different domains A–D corresponding to different signs of the wave number in the x and z space directions. (b) Direct space. A synthetic view of the four internal wave beams of the same frequency.c_p denotes the phase velocity and it is parallel to the wave vector k and orthogonal to its associated group velocity c_g.

3.2.4   Hilbert transform

With synthetic schlieren we are able to visualise the internal waves and with Digiflow we are able to get the perturbation gradient fields. We further analyse these by performing a Fourier transform and get the spectra of the internal waves (Hazewinkel, 2008) ; however no direct information is given on   the direction of propagation   of the waves. The direction of propagation becomes important for the corrugated wall experiments where scattering of the waves on the boundaries will be significant. A demodulation technique with which the direction of propagation of the wave beams can be distinguished is the Hilbert transform (HT). This method has been applied to internal waves in two-dimensional fluids for the first time by Mercier et al (2008). The Hilbert transform allows for the discrimination of the different possible directions of an internal wave beam associated with one given frequency. There are four possible directions for one given frequency, that is one angle of propagation. The beams can be discriminated by their wave vector, k_x, k_z , according to the sign of both components, so when both the wave vectors are positive the propagation is upward and rightward, if both are negative then the propagation is downward and leftward, and for the

two remaining cases it is upward and leftward for $k_x < 0$ and $k_z > 0$, and downward and rightward for $k_x > 0$ and $k_z < 0$, (see also fig 3.10).

The steps followed to perform a Hilbert analysis are the following:

1. Perform harmonic analysis over a time equal to at least one period of oscillation and pick the forcing frequency. Based on this, reconstitute the filtered perturbation density time series.
2. Perform a spatial two-dimensional Fourier transform of this perturbation density field as a function of time.
3. Apply a selective band filter in Fourier space by choosing one of the aforementioned, k_x, k_z, quadrants. In this step the four directions of propagation are isolated.
4. Perform an inverse Fourier transform and move back to the real space.

Chapter 4

The default experiment

In this chapter the default experiment is described. This experiment was realized in the smooth two-dimensional trapezoidal basin described in chapter 3 with a linear stratification. We outline the procedure followed for all the experiments performed. The results of this experiment are also used as a reference for comparison with the perturbation cases described in the following chapter.

4.1 Experiment outline

The experiment consisted of two parts. The oscillation phase and the decay phase. We oscillated the platform for 50 periods with a forcing frequency $\omega = 1.26\ rad\ s^{-1}$ and a forcing amplitude of horizontal displacement A=0.02 m; after 50 periods the oscillation was terminated and the attractor was left to decay. During the oscillation phase we observed the built up of the attractor. The generated basin scale waves (low wave number) from the sloping wall were being focused until the smallest waves (high wave number) reached the viscous length-scale, l, ($\sim O(10)\ mm$) and a balance was attained. The viscous length scale is defined as: $l_v = (gv)^{1/3}/N$, (e.g Sutherland et al. 1999), where v is the kinematic viscosity ($v = 1mm^2s^{-1}$). This process lasted about twenty periods and from that moment on the attractor was in steady state. At $t = 50T$ the attractor was left to decay by terminating the oscillation of the tank.

During the oscillation phase 16 frames per period were captured. On the perturbation gradient density field measured by synthetic schlieren, we performed harmonic analysis (from here on referred to as HA) over the last oscillation period. From the HA we obtained a complex field from which both the amplitude and phase show the attractor, see figure 4.1. The HA amplitude and phase are presented for the b_x component. In the amplitude figure, the decay of the wave amplitude in the beams due to viscosity is observed in the clockwise direction starting at the sloping wall (Hazewinkel et al. 2008). In the phase figure, the shear motion in the beams becomes visible. The colorbar in both plots is going to be used for most of the figures presented in chapter 5. We also present the output of the ray tracing model for the physical parameters of the experiment (see table 4.1) for a direct comparison with the observations. The wave beams that make up the attractor are from now on called branches and in a clockwise manner starting from the sloping wall are referred to as 1st, 2nd etc. The white lines, sections S1 to S4, intersecting the attractor branches perpendicularly, define the coordinate system and are indicative of the sampling lines used to obtain the wave number spectra.
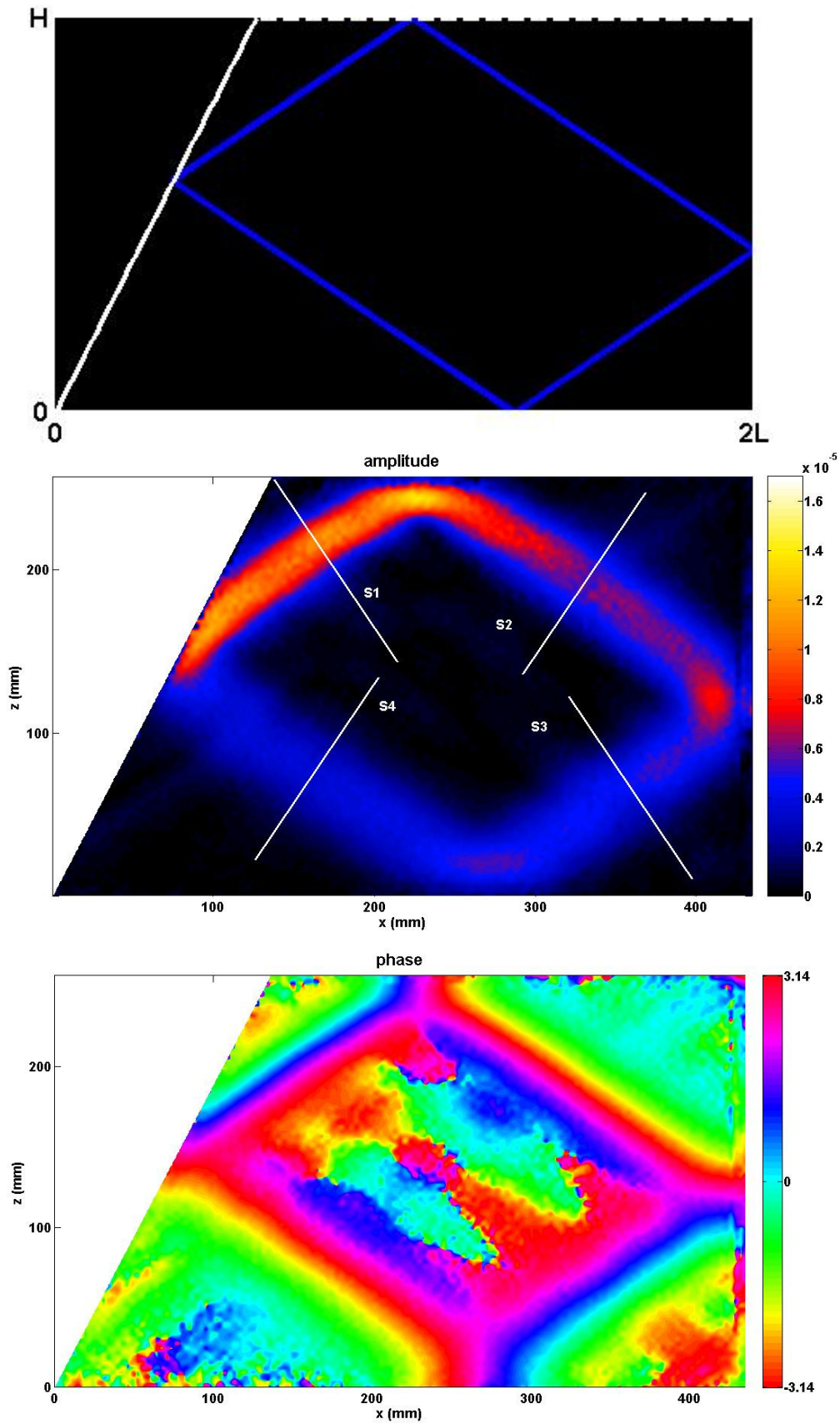
Figure 4.1 Ray tracing for the default experiment parameters. Amplitude and phase from observations from HA. The colorbars in this figure will be the same in the following plots.

Basin length	$2L$	**453**	***mm***
Fluid height	H	255	mm
d Parameter	d	-0.42	
Forcing frequency	ω	1.26 ($2\pi/4.98$)	$rad\ s^{-1}$
Forcing amplitude	A	20	mm
Buoyancy frequency	N	2.25	$rad\ s^{-1}$

Table 4.1 Parameters for the default experiment

4.2 Spectral evolution

To get the wave number spectrum of the attractor we introduce a new coordinate system (η, ξ) that aligns with the branches and the wave vector, **k**, in the (x, z) plane. The (η, ξ) system is redefined for each branch of the attractor; η is the coordinate normal to the attractor branch and along the white section shown in figure 4.1. For each section (S1 − S4) η is given by:

$$\eta_1 = +x \cos\theta - z \sin\theta$$
$$\eta_2 = -x \cos\theta - z \sin\theta$$
$$\eta_3 = -x \cos\theta + z \sin\theta$$
$$\eta_4 = +x \cos\theta + z \sin\theta,$$

where θ is the angle of the 1st attractor branch with the vertical. In this way the buoyancy gradient along the η direction for the first branch, for example, is defined as:

$$b_{1\eta} = b_x \cos\theta - b_z \sin\theta.$$

We then applied a Fourier transform around the forcing frequency along the white line sections $S1$ to $S4$ (η direction) that are shown in figure 4.1. The lines are perpendicular to the lines of constant phase so the wave number, **k**, can be resolved.

In figure 4.2 the spectra of all the branches are plotted for $t = 50T$. As we move from $S1$ to $S4$, we clearly see the diminishing of the spectral peak power and its predicted shift towards low wave numbers (Hazewinkel et al., 2008) which is indicative of the viscous processes acting on the small wavelengths of the attractor branches. Comparing to the similar figure $1.6(a)$, we observe the same pattern. The dominant wavenumber in this case is slightly greater than in figure $1.6(a)$. This difference could be attributed to the different fluid height, H, and stratification, N, used in the two experiments; these two parameters together with the kinematic viscosity, v, set the value of the dominant wavenumber. We also plot the evolution of the wave number spectra during the whole oscillation period (figure 4.3). There the gradual built up of the attractor can be seen; until about t=20T the spectrum grows from low to high wave numbers and then it reaches equilibrium (steady state).

4.3 Hilbert Transform (HT)

To investigate the direction of propagation of the waves in the attractor we apply the Hilbert transform method, as described in chapter 3, to the harmonically analyzed buoyancy gradient field. With this method it is possible to discriminate the direction of a wave beam by identifying the sign of the wave vectors k_x, k_z. The filtered images of figure 4.4 show in detail the four directions of energy propagation for the default experiment attractor. From here on
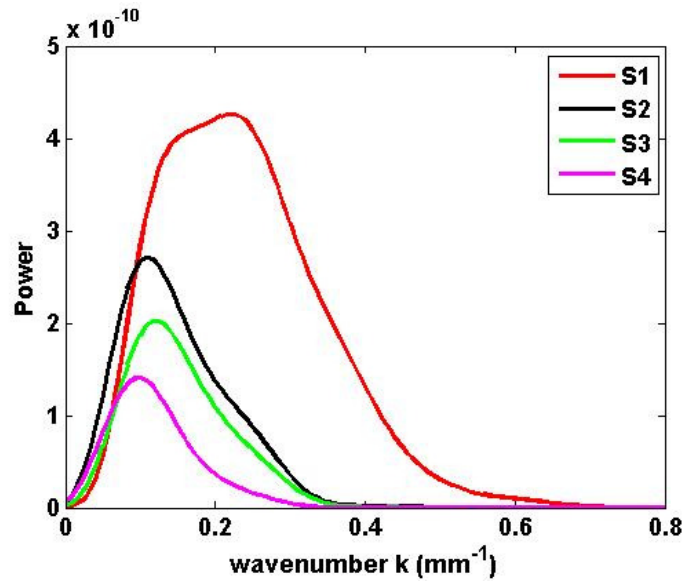
Figure 4.2 Wave number spectra for the four attractor branches S1-S4 of the default experiment at $t = 50T$ along the white sections visible in figure 4.1
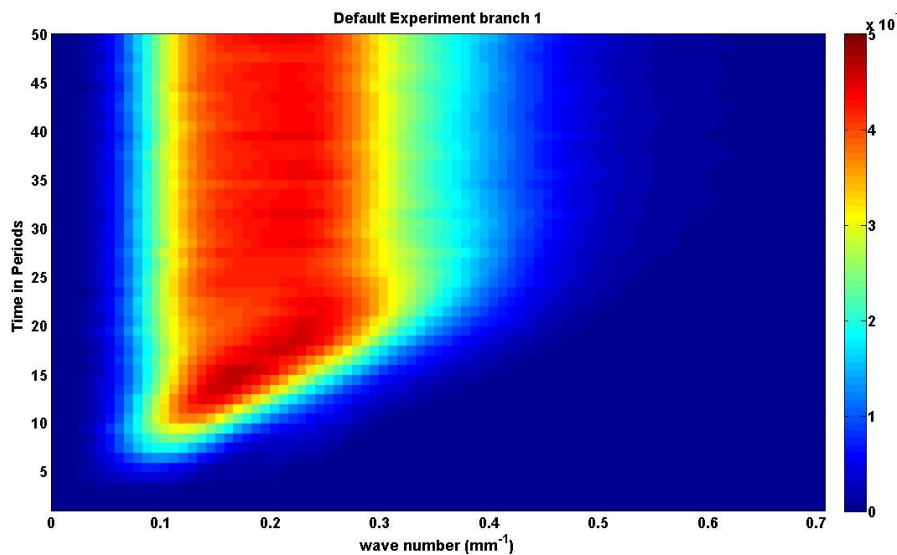

Figure 4.3 Evolution of the wave number spectra along section S1 during the whole oscillation period (t=1:50 T). Notice that the colorbar used here is not scaled as figure 4.1

we are going to denote the direction of energy propagation as A for ($k_x > 0$, $k_z < 0$), B for ($k_x > 0$, $k_z > 0$), C for ($k_x < 0$, $k_z > 0$) and D for ($k_x < 0$, $k_z < 0$). In this case the attractor branches are mono-directional, meaning that the energy in each branch propagates only in one direction. If backscattering was taking place this would not have been the case.

4.4 Superposition of spectra

We apply a Fourier transform on the Hilbert filtered data similar to the one described in section 4.2. Then we superimpose the obtained spectra to the one shown in figure 4.2. This is done for each branch separately. In the ideal case of no backscattering, as the default experiment, the spectrum of the 1st branch (along S1) should be represented only from the A
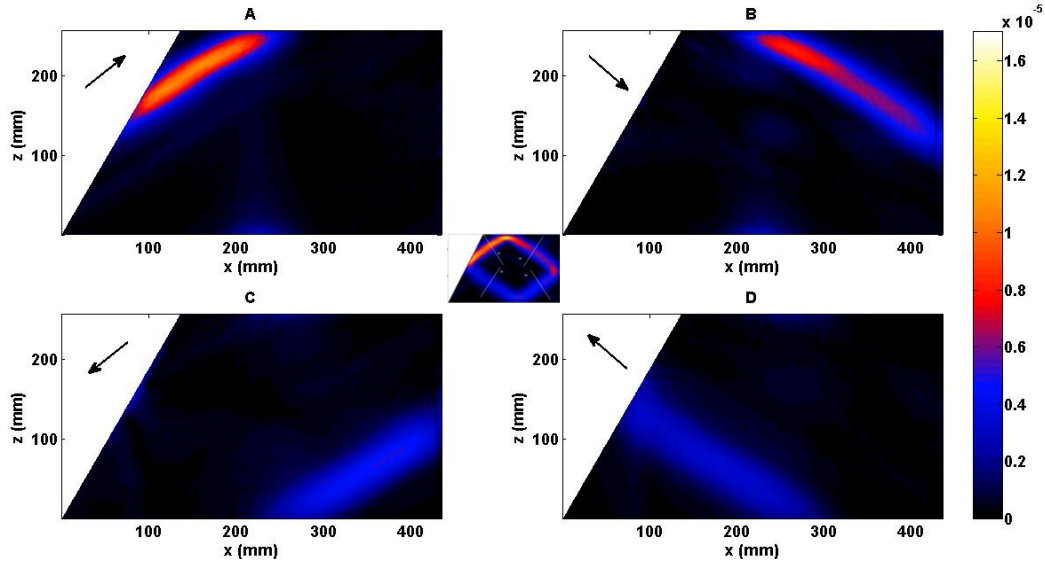
Figure 4.4 Hilbert transform for the default experiment showing the four propagation directions. In A: $k_x > 0$, $k_z < 0$, in B: $k_x > 0$, $k_z > 0$, in C: $k_x < 0$, $k_z > 0$, in D: $k_x < 0$, $k_z < 0$.
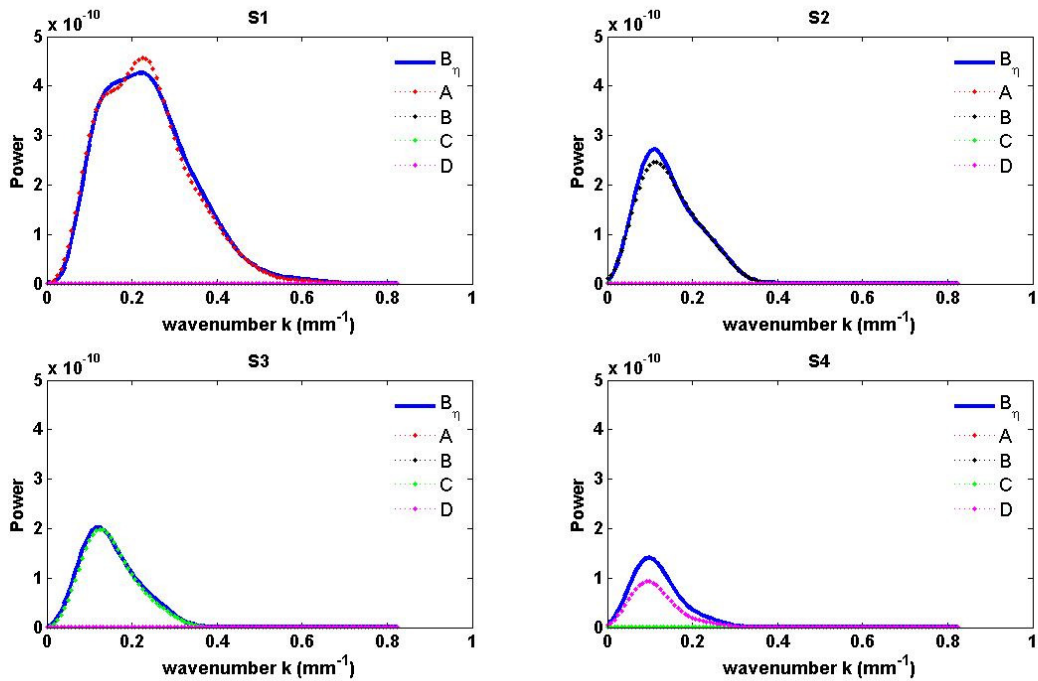

Figure 4.5 Superposition of wave number spectra of the four attractor branches S1-S4 with the wave number spectra after the filtering with Hilbert transform. The blue solid line indicates the wave number spectra before the filtering. The dotted coloured lines indicate the wave number spectra after the filtering, red is used for quadrant A, black for B, purple for C and green for D.

spectrum, the 2nd only from B and so on. This can be seen in figure 4.5. In this figure there is a clear match between the energy directions and the branches. We observe a slight mismatch regarding the power of the superimposed spectra; the power of the HT spectra possibly depends on how the selection is done in the Fourier space. However, this mismatch is not very important here as our prime interest is in matching to each wavenumber peak a direction of propagation. The peak wavenumber of each branch is clearly indicated by the filtered data.

Chapter 5

Perturbations

Following the procedure described for the default experiment we investigate the behaviour of the fluid when perturbations are present. First we scan the basin with a series of forcing frequencies, then we fill the tank with a non uniform, three layer type of stratification and at last we perturb the geometry of the tank by introducing corrugated sidewalls. A discussion for each set of experiments accompanies the presentation of the results.

5.1 Frequency scan

In a smooth tank filled with linearly stratified water of $N = 2.15 \ rad \ s^{-1}$, we perform a series of experiments in which we vary the frequency. By varying the frequency the τ parameter is changing and different attractors are established following the bird eye view diagram of figure 2.1. We use ray tracing to simulate the experiments and its results are shown next to the amplitude and phase obtained by harmonically analysing the last four periods of the oscillation (figure 5.1). In general ray tracing is in good agreement with the observations. The parameters of all the experiments are shown in table 5.1. The experiments are coded as FS# (Frequency Scan + number of experiment). We aim in checking both the (1,1) and the (2,1) attractor regions visible in figure 2.1. For this we start with a low frequency and we subsequently move to higher values.

The FS1 experiment reveals the first attractor found in the (1,1) region. The amplitude of this attractor compared to the default experiment is very weak but the phase structure is clear. By looking at the ray tracing of this experiment we find a slight disagreement. This points out the limitations of ray tracing when used to simulate the experiments. Ray tracing is sensitive to changes in the τ parameter, which is a function of the stratification and forcing frequency; given the uncertainties in the observations, typically at the order of a few percent, ray tracing gives an approximate idea of the position of the attractor. The FS2 experiment gives a clear (1,1) attractor, similar to the one in the default experiment. The FS3 is again a (1,1) attractor, however, the amplitude and phase do not clearly reveal the four branches. For this, we perform a Hilbert transform which clarifies the clockwise direction of energy propagation. In the filtered figure 5.2, the four branches can be distinguished. The ray tracing for FS4 and FS5 reveals complicated attractor shapes. However, the amplitude and phase structures of these experiments give a distinguishable signal in the regions that the rays are dense. Finally the attractor of FS6 is a (2,1) attractor with a clear signal. We also perform a Hilbert transform for
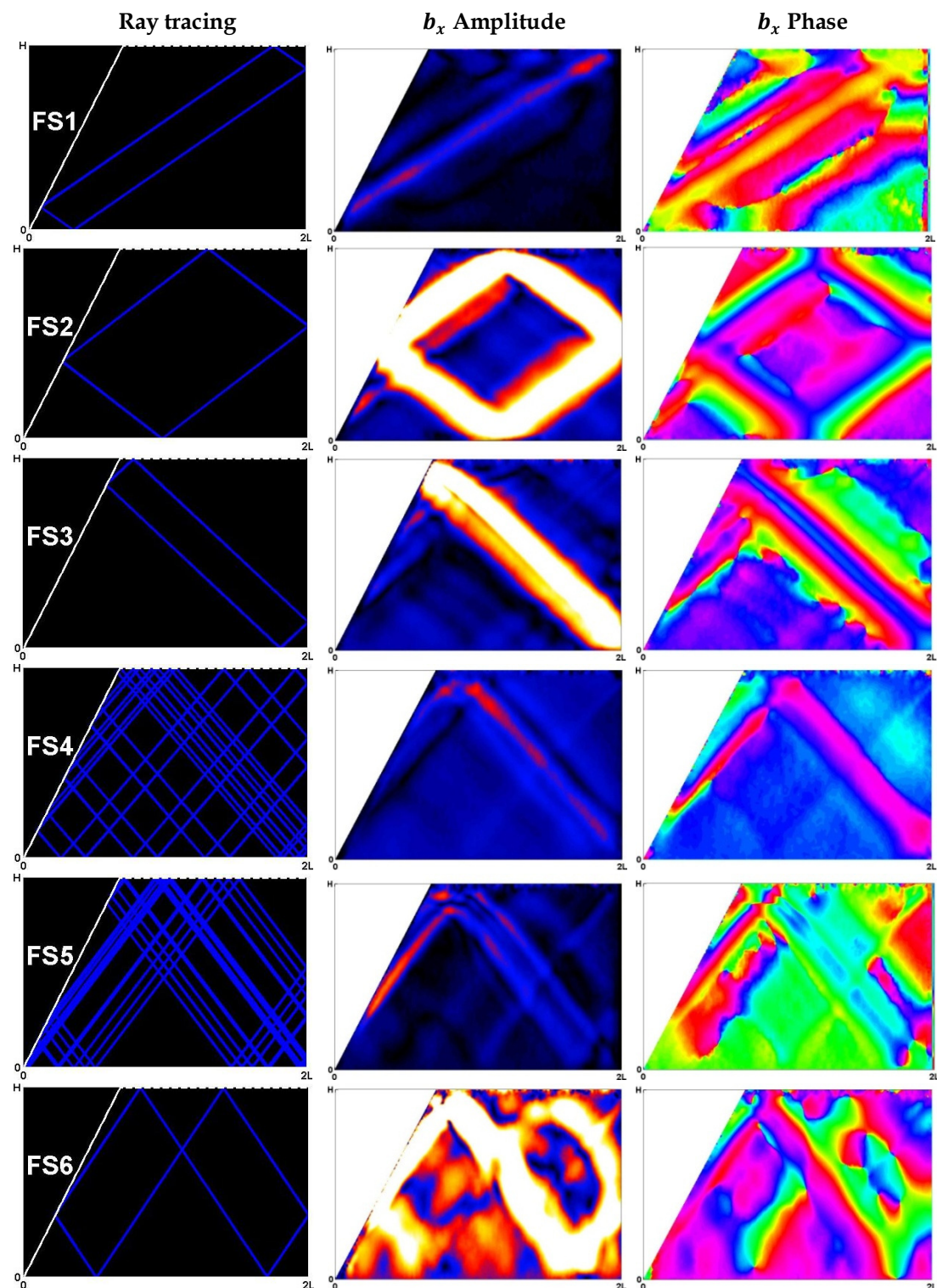
Ray tracing	b_x Amplitude	b_x Phase

Figure 5.1 Overview of the frequency scan experiments. Ray tracing, b_x amplitude and b_x phase are shown for the range of frequencies used. For experiment parameters see table 5.1

this attractor to show the direction into which the energy propagates subsequently along the branches labelled 1-6, that make up this attractor (figure 5.3).
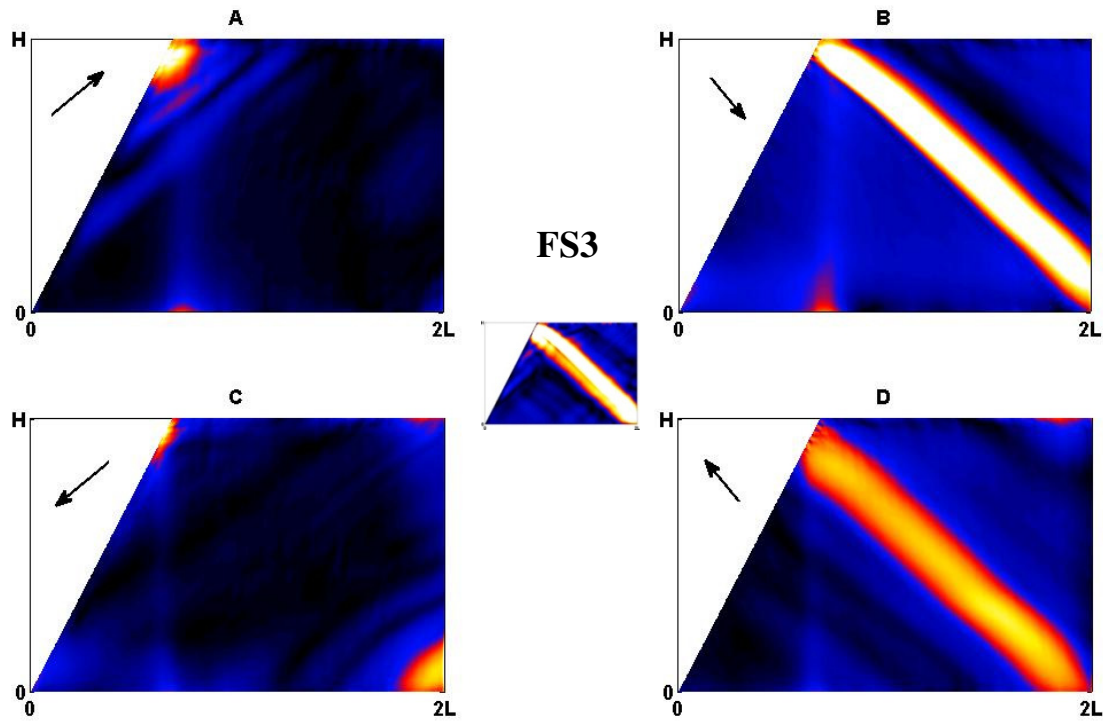
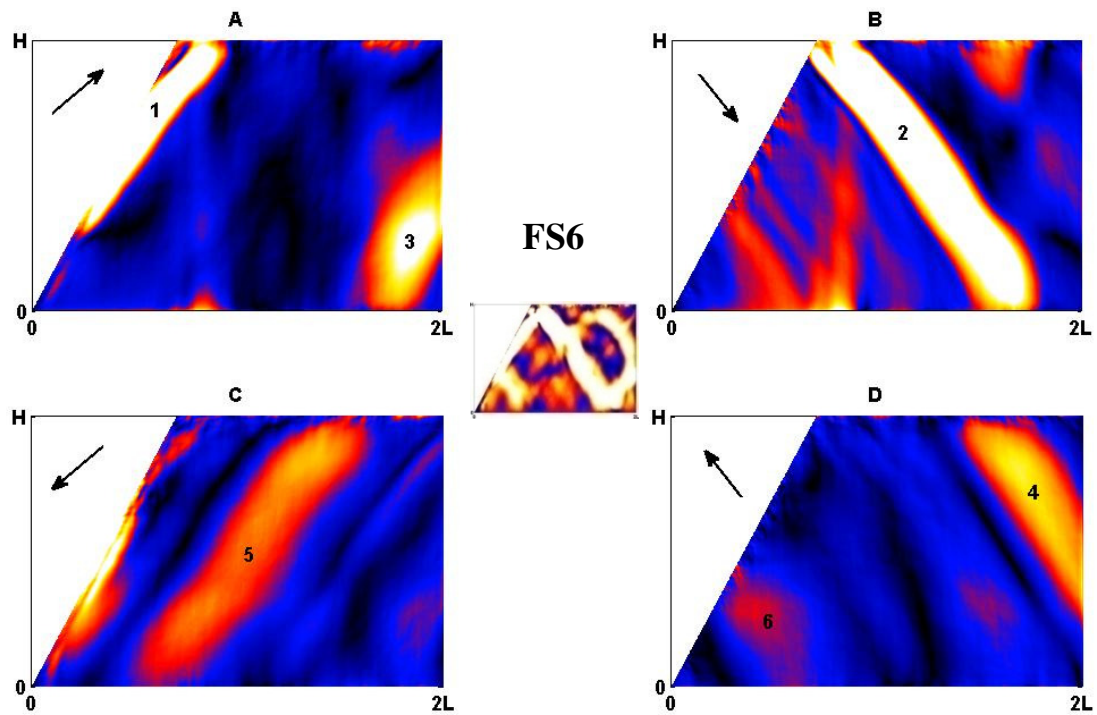*Figure 5.2 Hilbert Transform of the FS3 experiment, revealing the four branches of the attractor.*

Figure 5.3 Hilbert transform of the FS6 experiment showing the branches of a (2,1) attractor.

Basin length	$2L$	**453**	***mm***
Fluid height	H	300	mm
d Parameter	d	-0.32	
Forcing amplitude	A	20	mm
Buoyancy frequency	N	2.15	$rad\ s^{-1}$
Forcing frequency	ω		
FS1		$1.22\ (2\pi/5.14)$	$rad\ s^{-1}$
FS2		$1.31\ (2\pi/4.80)$	$rad\ s^{-1}$
FS3		$1.47\ (2\pi/4.28)$	$rad\ s^{-1}$
FS4		$1.63\ (2\pi/3.86)$	$rad\ s^{-1}$
FS5		$1.71\ (2\pi/3.68)$	$rad\ s^{-1}$
FS6		$1.78\ (2\pi/3.52)$	$rad\ s^{-1}$

Table 5.1 Parameters for the frequency scan experiments

5.2 Non uniform stratification

The tank is filled with a three-layer, smooth transition stratification as described in chapter 2 (see figure 3.3) and it is oscillated with a frequency of $\omega = 1.3\ rad\ s^{-1}$. The top and bottom layers have the same stratification. Despite the presence of the middle layer an attractor is established; we present the amplitude and phase structures in figure 5.4. Because the amplitude is much weaker than the default experiment we use a different colorbar scale, set an order of magnitude lower than the one used in the rest of the experiments. The ray tracing model assumes a uniform stratification so it is not used for this experiment. The parameters of the experiment are shown in table 5.2.

The propagation angle of the internal waves depends on the stratification so the attractor does not have a simple structure anymore. The branches appear to be curved, indicating the smooth stratification transition between the layers. By taking a closer look we can distinguish the shape of two attractors, normal to each other. However, this might be associated with transmission and partial reflection at the interface of the layers (Nault & Sutherland, 2007). To have a qualitative view of what kind of effects are taking place, we filter the HA field to detect the directions of energy propagation, shown in figure 5.5. Only one attractor is clearly visible, with each branch changing its angle of propagation when it enters a different layer. A thinner beam starting from the top layer is visible in the A and B direction but it doesn't appear in C and D. This beam seems to contribute to the enhanced amplitude visible as reflection of the first attractor branch in the middle layer. This renders the existence of a wave beam being trapped in the middle layer less probable. The branches of the attractor are thin enough to be transmitted from one layer to the other with minimum reflection taking place.

5.3 Sawtooth topography

We perform a series of experiments in which sawtooth sidewalls with varying number of corrugations are inserted in the wall opposite to the slope. We start with a small perturbation and subsequently move to larger ones. The characteristics of the corrugations are shown in table 3.1 and the parameters of each experiment are shown in table 5.3. The experiments are coded as ST# (Sawtooth topography + number of experiment).

Basin length	$2L$	**453**	***mm***
Fluid height	H	290	mm
Middle layer height	h	50	mm
Forcing amplitude	A	20	mm
Forcing frequency	ω	1.3 $(2\pi/4.8)$	$rad\ s^{-1}$
Stratification			
top layer	N_t	1.8	$rad\ s^{-1}$
middle layer	N_m	3	$rad\ s^{-1}$
bottom layer	N_b	1.8	$rad\ s^{-1}$

Table 5.2 Parameters of the non uniform stratification experiment.
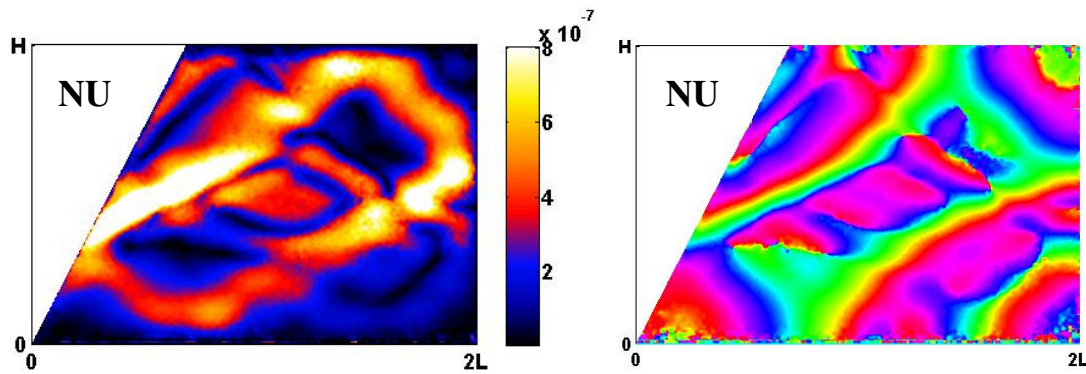
Figure 5.4 Amplitude and phase of the non uniform stratification experiment.
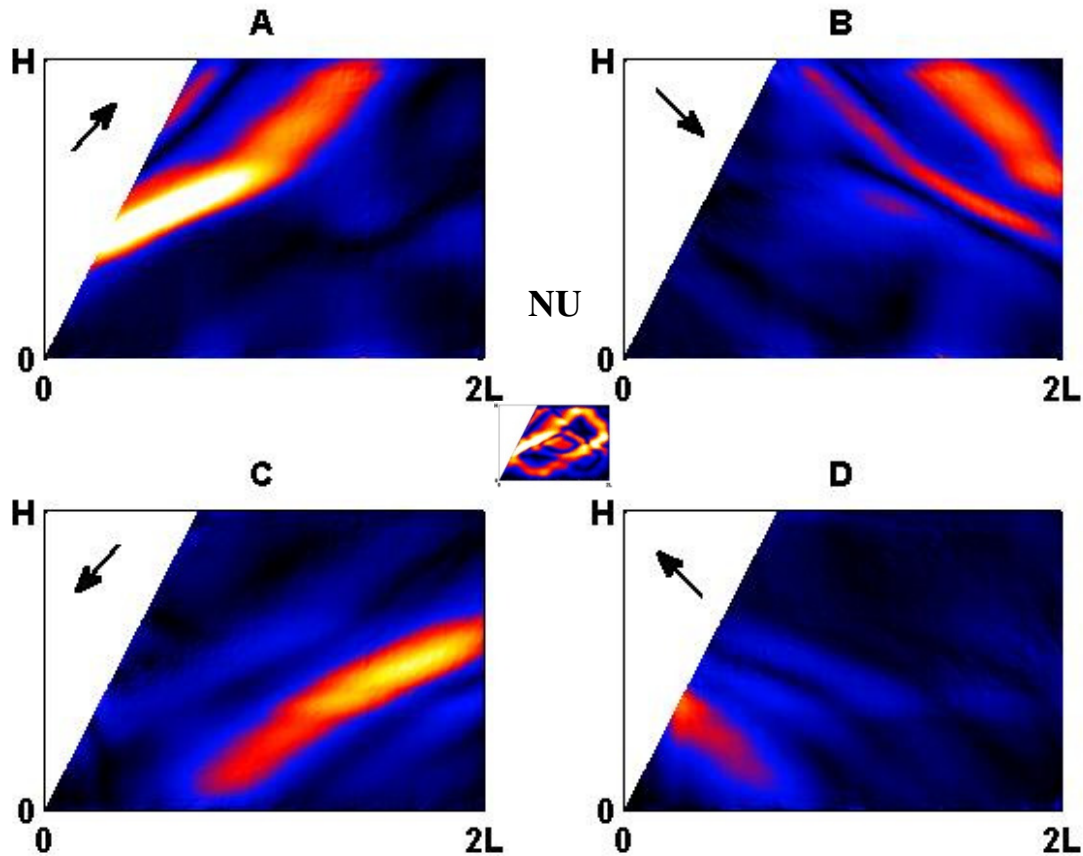
Figure 5.5 Hilbert transform of the non uniform stratification experiment

33

Basin length	$2L$	**453**	***mm***
Forcing amplitude	A	20	*mm*
Fluid height	H		
ST1		300	*mm*
ST2		264	*mm*
ST3		260	*mm*
d Parameter	d		
ST1		-0.29	
ST2		-0.37	
ST3		-0.38	
Forcing frequency	ω		
ST1		$1.37\ (2\pi/4.57)$	*rad s*$^{-1}$
ST2		$1.26\ (2\pi/4.98)$	*rad s*$^{-1}$
ST3		$1.26(2\pi/4.98)$	*rad s*$^{-1}$
Stratification	N		
ST1		2.15	*rad s*$^{-1}$
ST2		2.19	*rad s*$^{-1}$
ST3		2.14	*rad s*$^{-1}$
Number of peaks	n		
ST1		*20*	
ST2		*7*	
ST3		*3*	

Table 5.3 Sawtooth experiments parameters. Note that the d parameters varies between the experiments because the height is different.

We use the ray tracing model to simulate the experiments and the results are shown next to the amplitude and phase obtained by harmonically analysing the last period of the oscillation (figure 5.6). Considering that the attractor occurrence is affected by the corrugations, as discussed in chapter two, we also plot the ray paths starting from multiple surface positions. Although ray tracing does not predict any backward scattering from the sawtooth boundary, the attractors from the model are in good agreement with the experiments as can be seen in figure 5.6. For all the experiments, we plot the superposition spectra and for specific cases we show the Hilbert analysis and the evolution of the spectra during the oscillation.

We start with a small perturbation with a sidewall of twenty peaks, experiment ST1. The attractor resembles the one in the smooth tank described at the default experiment chapter. The only immediate effect of the corrugation is visible in the attractor branches, which are not as smooth as in the default case. The perturbation does not influence the wavenumber spectra of the attractor, as shown in figure 5.7. A double peak in the frequency appears at the 1st branch; this, however, is not considered to be a direct effect of the corrugation as the energy direction is the same (clockwise) for both peaks. In the phase figure we can distinguish a beam parallel to the 1st branch; the second peak in the spectra of the 1st branch probably corresponds to this. No scattering, neither forward nor backward, is observed in this experiment. The length scale of the side wall is $l_c = 10mm$. As seen here, this is very small to produce waves that can propagate for a sufficient time, as to be visible as individual beams; if any waves are being produced they are shortly being dissipated.

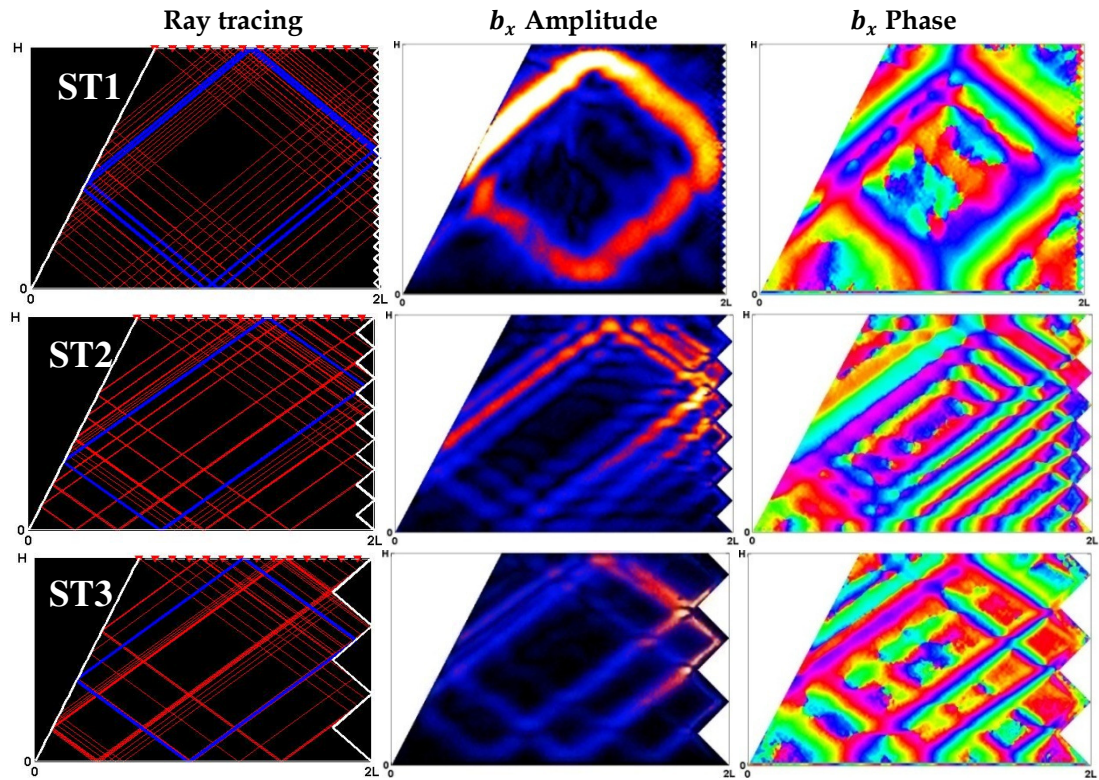| Ray tracing	b_x Amplitude	b_x Phase

Figure 5.6 Ray tracing, amplitude and phase of the sawtooth sidewall experiments. In the ray tracing figures the red lines depict the paths of rays starting from various surface points and the blue lines depict the resulting limit cycles.
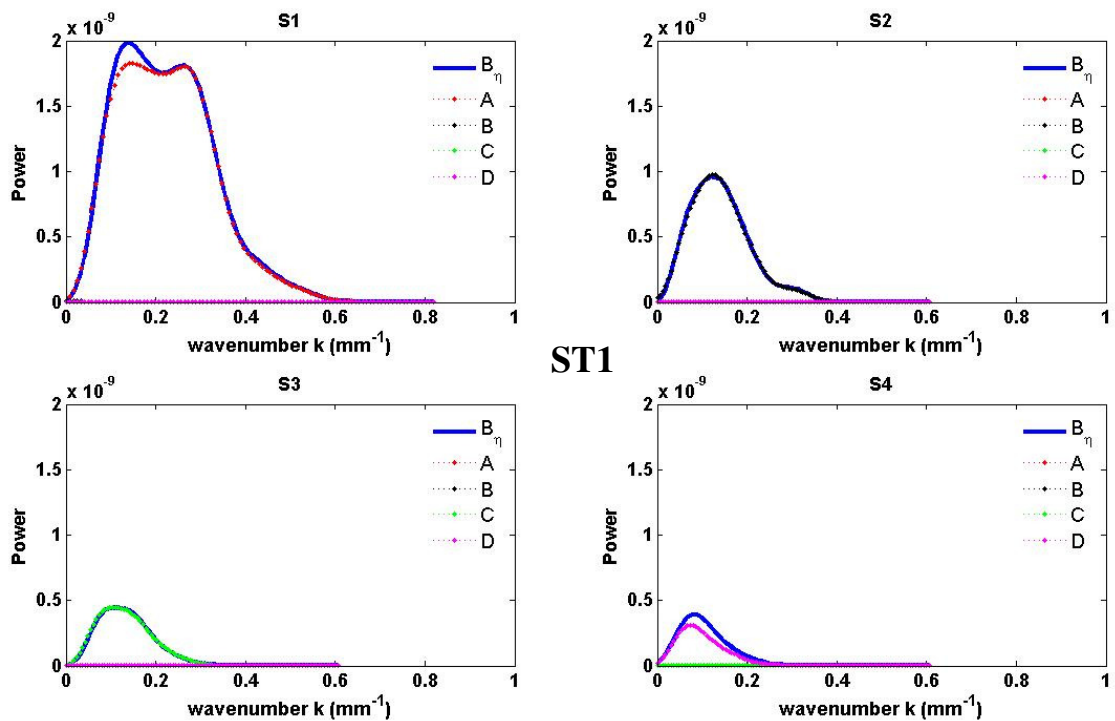

Figure 5.7 Superposition spectra for ST1. Each branch is mono-directional similarly to the default experiment.

35

In the next experiment, ST2, a sawtooth with 7 peaks seems to really perturb the fluid response. When the oscillation starts an intense activity is observed immediately at the topography, with waves generated at the peaks. However, the focused basin scale generated waves are the ones contributing to the observed pattern when the steady state is reached. The pattern is recognised as an internal wave attractor, but distorted. More specifically, the internal wave energy is still focussed around an attractor, but the corrugation at the sidewall, which has a length scale of $l_c = 38mm$, seems to break the beam structure of the branches.

The breaking of the beam structure is clearly seen in the spectral analysis (figure 5.9). The side walls introduce new dominant wavenumbers to the spectra. The dominant wavenumber in the 1st branch, $k_{1p} = 0.13 \, mm^{-1}$, is associated with the presence of the sloping wall. It can also be picked in the rest of the branches, subsequently diminishing in power, as expected, due to viscous effects. It is not, however, the dominant wavenumber in the 2nd and 3rd branches. There, the dominant wavenubers are associated with the sawtooth; in the 2nd branch it is $k_{2p} = 0.33 \, mm^{-1}$, and in the 3rd branch it is $k_{3p} = 0.39 \, mm^{-1}$. The filtered amplitude, where we can distinguish the directional components of the branches, is shown in figure 5.8. The superposition of the Hilbert spectra is shown in figure 5.9. With HT we can readily separate the incident from the reflected waves. In the superposition of spectra we observe that the energy direction of the dominant wavenumber in the 2nd branch, is away from the sawtooth. This indicates that backscattering is taking place. The backscattering is also visible in the 1st branch. Waves travelling in the anti-clockwise direction reflect at the surface contributing to the second wavenumber peak appearing in the 1st branch $k_{1sp} = 0.28 \, mm^{-1}$. The smaller value of k_{1sp} compared to k_{2p} is due to viscous effects. As the waves propagate, they are being dissipated, similarly to the viscous broadening observed in the branches of the smooth attractor. They propagate as individual beams along the 2nd branch, but viscous effects erase their structure when they have reached the 1st branch. Continuing their anti-clockwise propagation along the 1st branch, they reflect on the sloping wall where they are defocused by the slope. In the 3rd branch, the direction of the scattered energy is away from the sawtooth contributing constructively to the clockwise direction of the attractor. The power of the scattered wavenumber compared to the 2nd branch is lower. This suggests that backscattering is more significant than forward scattering. The scattered waves reflect at the bottom and appear in the 4th branch. Dissipation however has diminished their power to a level lower than the wavenumber of the attractor and by the time they reach the slope they have disappeared.

Next, we plot the evolution of the wavenumber spectra for the whole duration of the oscillation period, $t = 50T$, and for all the branches (figures 5.10 to 5.13). Note that the colorbar is different for each branch. In the 2nd branch the wavenumber associated with the sawtooth, k_{2p}, appears simultaneously to the wavenumber associated with the slope, k_{1p}. This suggests that the energy in the counter-clockwise direction is purely due to backscattering and not due to direct generation at the sawtooth. The same holds for the 3rd branch, with the difference that instead of backscattering the waves are scattered forward. At the 1st branch, the wavenumber associated with the sawtooth is established later than the attractor's, indicating its purely backscattering nature, as expected. The backscattered waves in the 1st branch appear about 5 periods after they do in the 2nd branch and they are much weaker. This is because dissipation processes are acting on it.
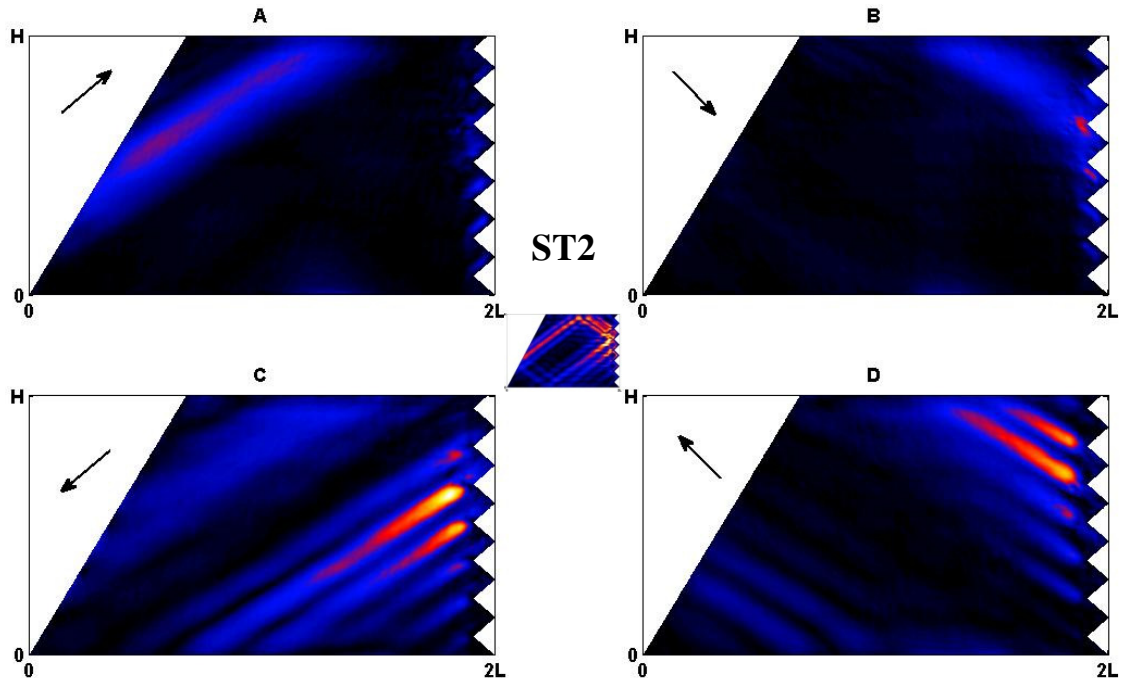
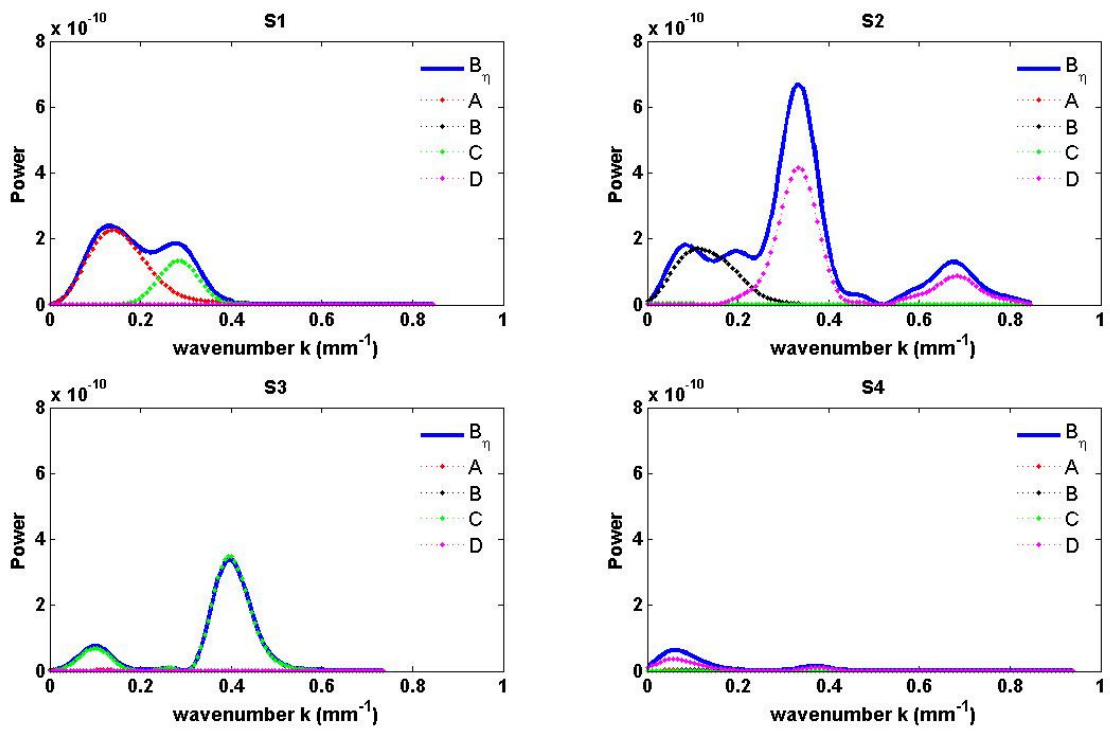*Figure 5.8 Hilbert transform of the ST2 experiment.*

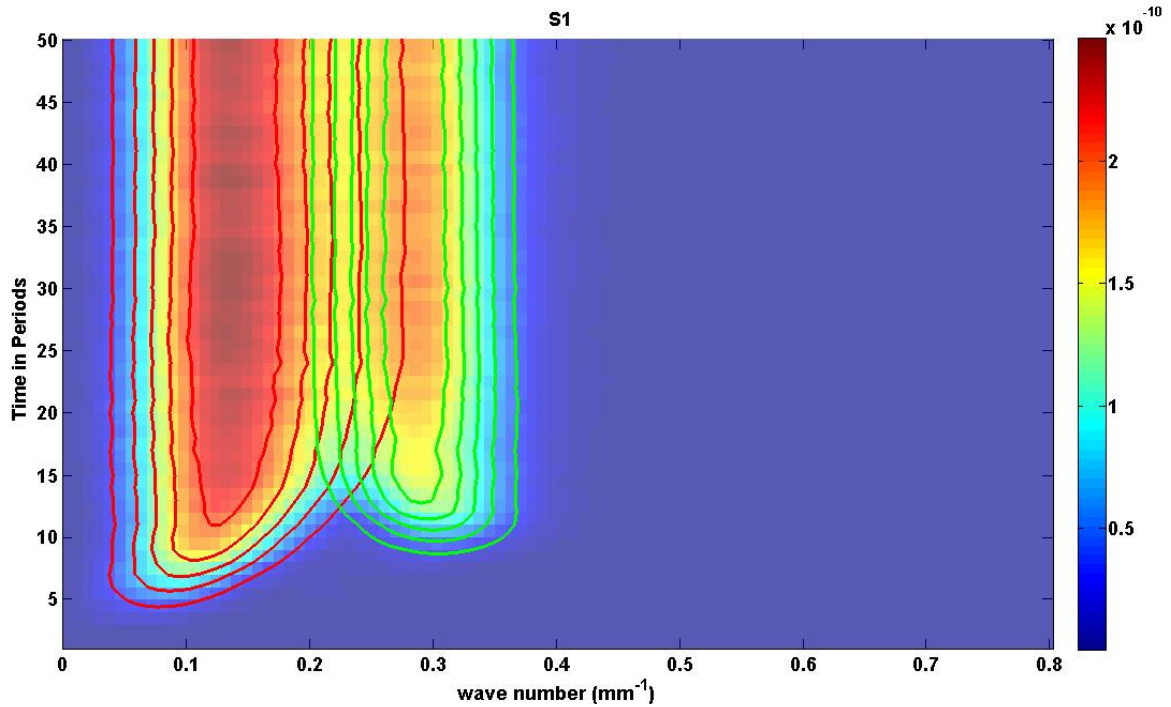*Figure 5.9 Superposition of spectra with the Hilbert transform spectra for ST2.*

Figure 5.10 Wavenumber spectral evolution for the oscillation period for the first branch of ST2. The contour lines are marking the evolution of the Hilbert spectra. The color coding of the contour lines is similar to figure 5.9 Red for the A component, Black for B, Green for C and purple for D.
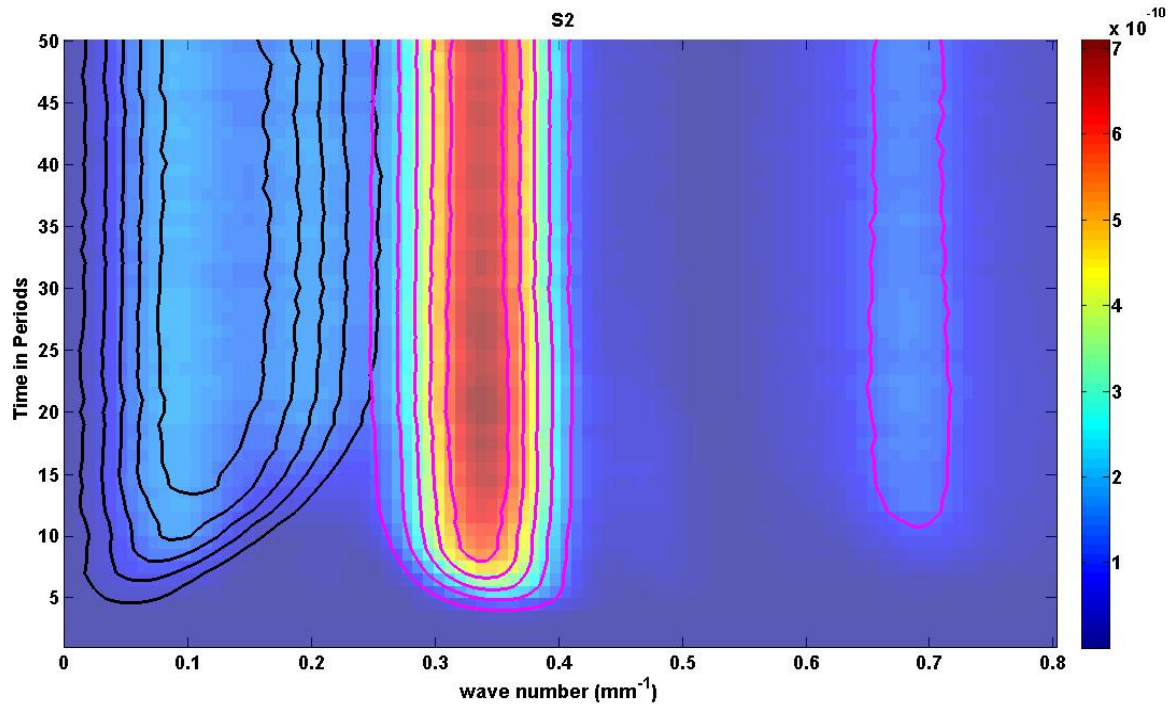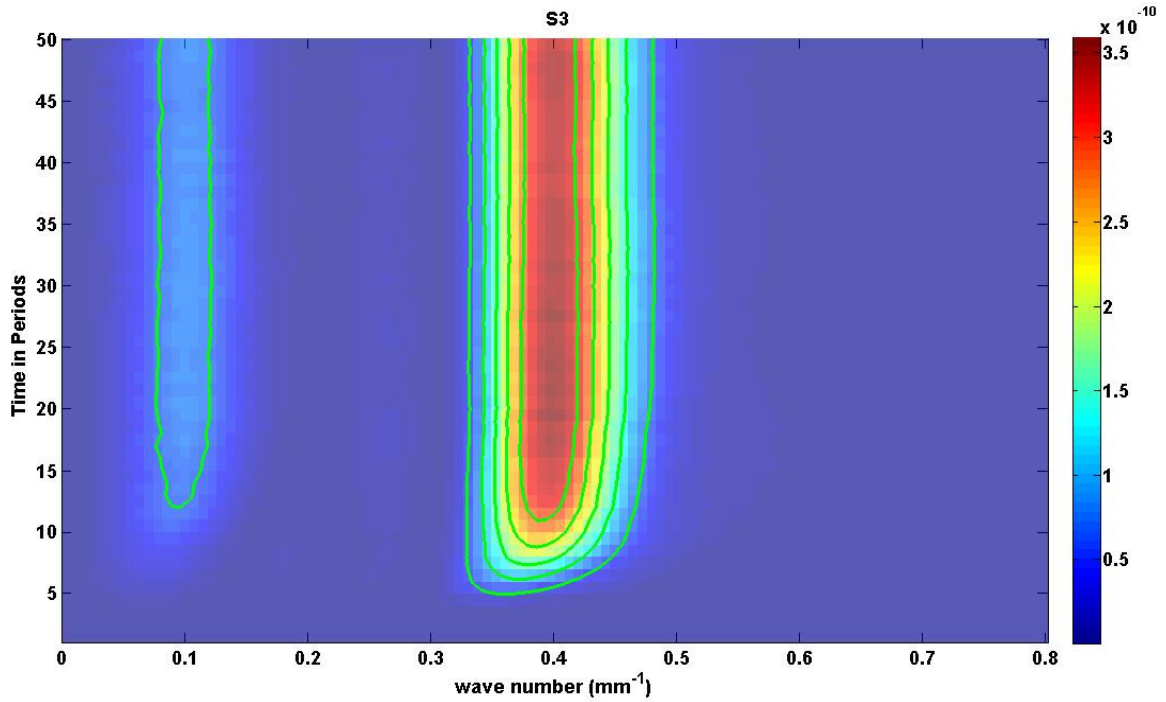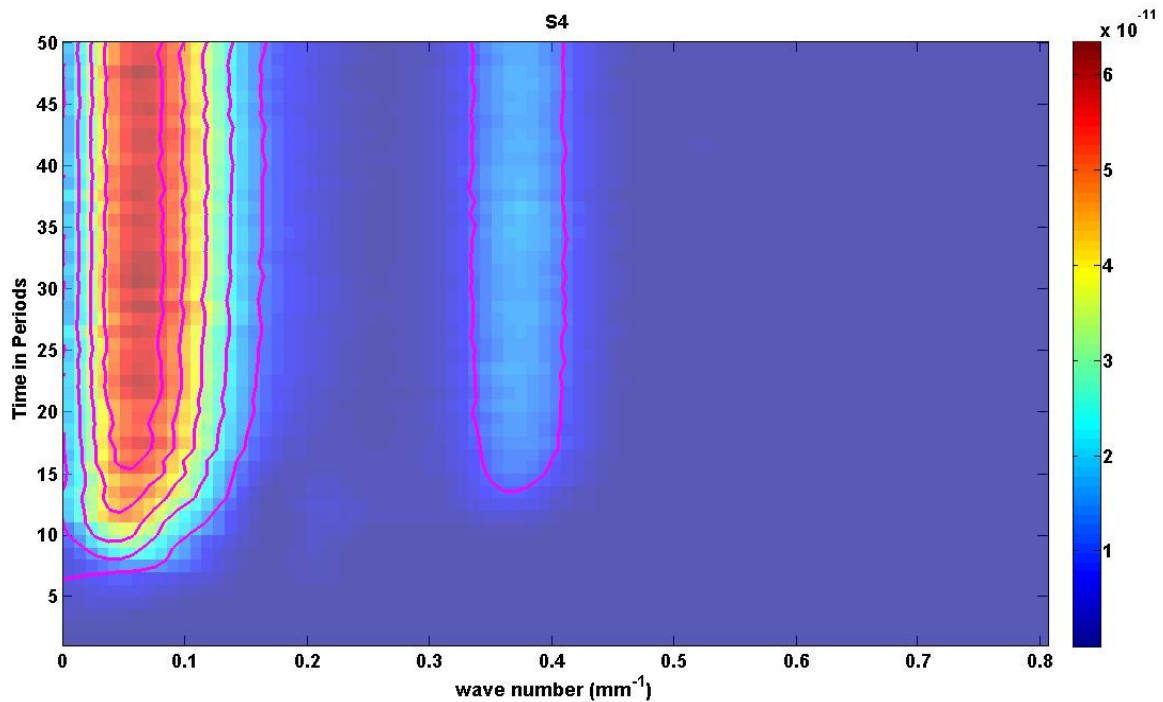

Figure 5.11 Wavenumber spectral evolution for the oscillation period for the second branch of ST2. The contour lines are marking the evolution of the Hilbert spectra. The color coding of the contour lines is similar to figure 5.9 Red for the A component, Black for B, Green for C and purple for D.

Figure 5.12 Wavenumber spectral evolution for the oscillation period for the second branch of ST2. The contour lines are marking the evolution of the Hilbert spectra. The color coding of the contour lines is similar to figure 5.9 Red for the A component, Black for B, Green for C and purple for D.
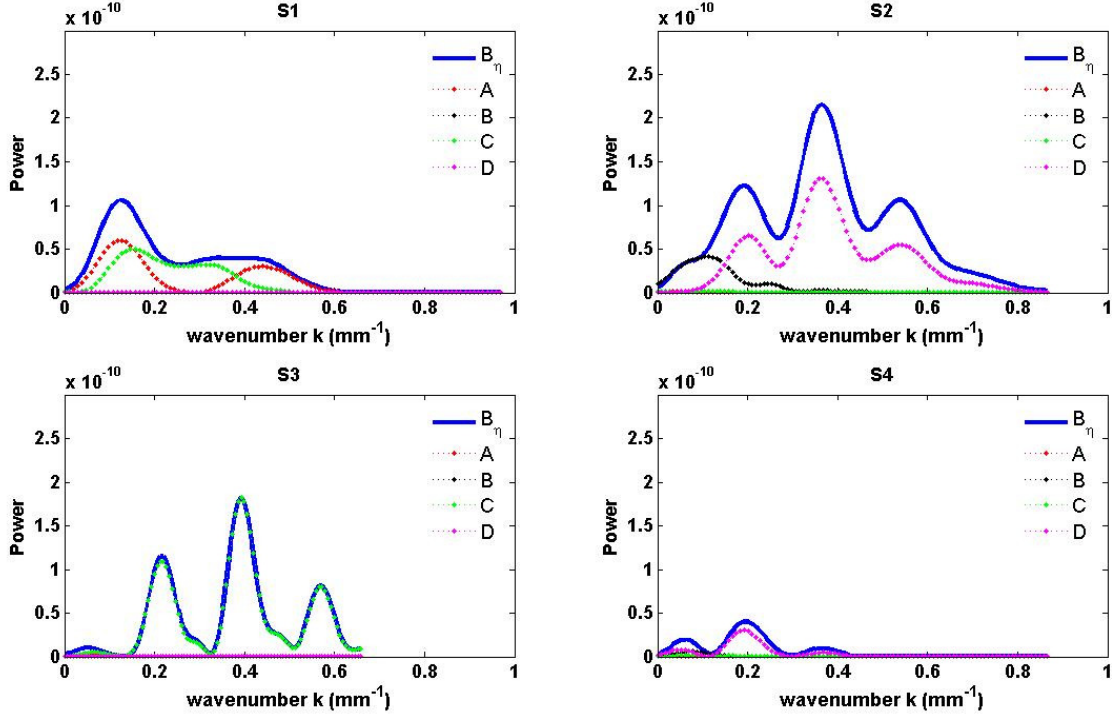

Figure 5.13 Wavenumber spectral evolution for the oscillation period for the second branch of ST2. The contour lines are marking the evolution of the Hilbert spectra. The color coding of the contour lines is similar to figure 5.9 Red for the A component, Black for B, Green for C and purple for D.

Figure 5.14 Superposition of spectra with the Hilbert transform spectra for ST3

Another notable point is the fluid between the sawtooth peaks. In figure 5.6 , an increased activity is observed which hints at mixing processes taking place at the boundary region. The mixed fluid spreads out horizontally. However the time scale is much smaller than the experiment time and does not affect the attractor shape.

In the ST3 experiment, the corrugation has three peaks but it also includes the first quarter of the fourth peak. Even though we used only three peaks in the ray tracing, the results are satisfactory (figure 5.6). The dense rays emanating from the topography edges are observed as the breaking of the attractor branches. The effects of the corrugation are similar to the ST2 experiment described before but they are much more pronounced. In figure 5.14 the superposition spectra are shown. The sawtooth associated wavenumbers are dominating the structure. The peak wavenumber of the 1st branch is $k_{1p} = 0.13 \ mm^{-1}$, similarly to ST2. The dominant peak wavenumber of the 2nd branch, associated with the sawtooth, is $k_{2p} = 0.37 \ mm^{-1}$, however two more peaks appear at $k_{2sp} = 0.19 \ mm^{-1}$ and $k_{2tp} = 0.53 \ mm^{-1}$. The spectra are heavily disturbed by the sawtooth and a detailed description of it becomes complicated. With the present means of analysis we can only speculate for some features. For example, the spectra of the 1st branch has a secondary peak corresponding to a clockwise propagation direction, at a higher than the dominant one wavenumber, $k_{1sp} = 0.43 \ mm^{-1}$. This could be a signature of the forward scattering at the sawtooth; the scattered waves with $k_{3sp} = 0.22 \ mm^{-1}$ in the 3rd branch reflect at the bottom and appear in the 4th branch with $k_{4p} = 0.19 \ mm^{-1}$. Subsequently, they reflect at the slope, where they are being focused, and appear at the 1st branch at a higher wavenumber $k_{1sp} = 0.43 \ mm^{-1}$. The focusing factor, $\gamma = \frac{\sin(\theta+a)}{\sin(\theta-a)}$ (e.g. Hazewinkel et al. 2008), for this experiment is $\gamma = 2$, which partially justifies the above assumption.

Chapter 5: Perturbations

What appears to be defining the extent that the sidewalls influence the attractor are: the length scale of the attractor, $2\pi/k_p$, the viscosity length scale, l_v, and the topography length scale, l_c. For the experiments presented here, the viscous length scale is estimated to be: $l_v = 10\ mm$, (see also section 4.1). The attractor length scale is 48 mm, for $k_p = 1.3\ mm^{-1}$.

If $l_c \leq l_v$, the sawtooth correlated internal waves are shortly dissipated and the attractor branches are unaltered. We observe this in ST1 with $l_c = 10mm$. If $l_c > l_v$, then, the sawtooth associated internal waves have a sufficient wavelength to propagate in the basin. They appear as individual beams that propagate along the attractor branches and they change the wavenumber spectra (see ST2 and ST3). The corrugation separates the attractor branches, with the maximum amplitude appearing along the centre of each beam rather than in the centre of the attractor branch. The individual beams propagate in a clockwise (forward scattering) or in a counter clockwise direction (backscattering) and are attenuated by viscosity. If $l_c < 2\pi/k_p$, the original shape of the attractor is preserved, (see ST2, $l_c = 38mm$), while if $l_c > 2\pi/k_p$, (see ST3, $l_c = 78mm$), the attractor branches are not clearly distinguished and the spectra are dominated by the wavenumber related to the corrugation. In all cases the wavenumber associated to the slope, is still traceable in all the braches

Chapter 6

Conclusions

In this chapter a summary of the conclusions of chapter two and chapter five is given.

In the simple domains of previous internal wave attractor observations, ray tracing was always used as a tool to find the attractor location. The present observations have shown that the use of ray tracing in distorted domains still can predict the position of the attractor, even when the perturbations are significant. It's weakness in not accounting for the backscattered components does not diminish its predictive power. Ray tracing reveals features of the distorted domains, like the occurrence of multiple attractors and the discontinuity of the bird eye view τ-x diagram.

Changing the forcing frequency led to a change in shape of the attractor. Although convoluted attractors imply regions of high shear, the fluid domain is not filled with shear regions. When the ray tracing shows a very complicated attractor, we find that some traces remain, especially in the phase of the HA. In general, the simpler the attractor, the stronger the fluid responds. The use of the Hilbert transform gave insight in the directional components of the complicated attractors.

Perturbations in stratification featured a noticeable fluid response when a simple attractor can be formed. The internal wave attractor initially grows by the ongoing focussing of large waves at the sloping wall starting from the weak sloshing of the water in the whole tank. Even with a non-uniform stratification the focussing at the sloping wall is not prevented by the middle layer and the attractor is formed.

Perturbations in the geometry of the domain with a corrugated sidewall raised the importance of the corrugation length scale. The attractors remain unaltered by corrugations whose length scale is smaller than the viscous wavelength. However, when the corrugation features approach the attractor's length scales, a spatial partitioning of the attractor branches is observed. Hilbert transform revealed the backscattered components at the topography and their contribution to the anticlockwise propagation.

We conclude that the fundamental response of a stratified fluid in a confined domain has to be described in terms of internal wave attractors. These attractors are influenced by the perfectness of the geometrical setting (stratification or domain) but they are still strongly present.

Bibliography

Baines, P. 1971 The reflexion of internal/ inertial waves from bumpy surfaces. J. Fluid Mech. 46, 273–291.

Benielli, D. & Sommeria, J. 1998 Excitation and breaking of internal gravity waves by parametric instability. J. Fluid Mech. 374, 117–144.

Dalziel, S. B., Hughes, G. O. & Sutherland, B. R. 2000 Whole field density measurements by 'synthetic schlieren'. Experiments in Fluids 28, 322-335.

Gerkema T. and Zimmerman J.T.F. 2008 An Introduction to internal waves, Lecture notes, Royal NIOZ.

Grisouard, N., Staquet, C., Pairaud, I. 2008. Numerical simulation of a two-dimensional internal wave attractor. J. Fluid Mech. 614, 1-14.

Hazewinkel, J., v. Breevoort, P., Dalziel, S. B., Maas, L. R. M. 2008. Observations on the wavenumber spectrum and decay of an internal wave attractor. J. Fluid Mech. 598, 373-382.

Hazewinkel, J., Grisouard, N., Dalziel, S. B. 2009. Comparison of laboratory and numerically observed scalar fields of an internal wave attractor. Preprint submitted to Elsevier.

Leblond, P. H., & Mysak, L. A. 1978 Waves in the ocean. Elsevier.

Lighthill, M. 1978 Waves in fluids. Cambridge University Press.

Longuet-Higgins, M. 1969 On the reflexion of wave characteristics from rough surfaces. J. Fluid Mech. 37, 231–250.

Maas, L. R. M. & Lam, F.-P. A. 1995 Geometric focusing of internal waves. J. Fluid Mech. 300, 1–41.

Maas, L. R. M. 2005 Wave attractors: Linear yet nonlinear. Int. J. Bifurcation and Chaos 15 (9), 2757-2782.

Maas, L. R. M., Benielli, D., Sommeria, J. and Lam, F. P. A. 1997 Observation of an internal wave attractor in a confined, stably stratified fluid. Nature, 388:557-561.

Marshall, J., Adcroft, A., Hill, C., Perelman, L., Heisey, C., 1997. A finite volume, incompressible Navier Stokes model for studies of the ocean on parallel computers. Journal of Geophysical Research 102, 5753-5766.

Mercier, M. J., Garnier, N. B., Thierry Dauxois, T. 2008, Reflection and diffraction of internal waves analyzed with the Hilbert transform, Phys. Fluids 20, 086601.

Nye, A. 2009 Scattering of internal gravity waves. PhD thesis, Cambridge University.

Sutherland, B., Hughes, G., Dalziel, S. & Linden, P. 2000 Internal waves revisited. Dyn. Atmos. Oceans 31, 209–232.

van Breevoort, P. 2008 Experiments on internal wave attractors, MSc thesis, Utrecht University.

Acknowledgements